Thesis for the Degree of Doctor of Philosophy

Modeling Approaches for Active Antenna Transmitters

Parastoo Taghikhani

CHALMERS

Chalmers University of Technology
Department of Microtechnology and Nanoscience (MC2)

Göteborg, Sweden 2021

Modeling Approaches for Active Antenna Transmitters

Parastoo Taghikhani

ISBN: 978-91-7905-603-2

Doktorsavhandlingar vid Chalmers tekniska högskola
Ny serie nr 5069
ISSN 0346-718X

Chalmers University of Technology
Department of Microtechnology and Nanoscience (MC2)
Microwave Electronics Laboratory
SE–412 96 Göteborg
Sweden
Telephone: +46 (0)31 – 772 1000
Email: parastoo@chalmers.se; parastoo.taghikhani@gmail.com

Typeset by the author using LaTeX.

Chalmers Reproservice
Göteborg, Sweden 2021

To my family

Abstract

The rapid growth of data traffic in mobile communications has attracted interest to Multiple-Input-Multiple-Output (MIMO) communication systems at millimeter-wave (mmWave) frequencies. MIMO systems exploit active antenna arrays transmitter configurations to obtain higher energy efficiency and beamforming flexibility. The analysis of transmitters in MIMO systems becomes complex due to the close integration of several antennas and power amplifiers (PAs) and the problems associated with heat dissipation. Therefore, the transmitter analysis requires efficient joint EM, circuit, and thermal simulations of its building blocks, i.e., the antenna array and PAs. Due to small physical spacing at mmWave, bulky isolators cannot be used to eliminate unwanted interactions between PA and antenna array. Therefore, the mismatch and mutual coupling in the antenna array directly affect PA output load and PA and transmitter performance. On the other hand, PAs are the primary source of nonlinearity, power consumption, and heat dissipation in transmitters. Therefore, it is crucial to include joint thermal and electrical behavior of PAs in analyzing active antenna transmitters.

In this thesis, efficient techniques for modeling active antenna transmitters are presented. First, we propose a hardware-oriented transmitter model that considers PA load-dependent nonlinearity and the coupling, mismatch, and radiated field of the antenna array. The proposed model is equally accurate for any mismatch level that can happen at the PA output. This model can predict the transmitter radiation pattern and nonlinear signal distortions in the far-field. The model's functionality is verified using a mmWave active subarray antenna module for a beam steering scenario and by performing the over-the-air measurements. The load-pull modeling idea was also applied to investigate the performance of a mmWave spatial power combiner module in the presence of critical coupling effects on combining performance.

The second part of the thesis deals with thermal challenges in active antenna transmitters and PAs as the main source of heat dissipation. An efficient electrothermal modeling approach that considers the thermal behavior of PAs, including self-heating and thermal coupling between the IC hot spots, coupled with the electrical behavior of PA, is proposed. The thermal model has been employed to evaluate a PA DUT's static and dynamic temperature-dependent performance in terms of linearity, gain, and efficiency. In summary, the proposed modeling approaches presented in this thesis provide efficient yet powerful tools for joint analysis of complex active antenna transmitters in MIMO systems, including sub-systems' behavior and their interactions.

Keywords: Active antenna transmitter, hybrid beamforming, active subarray antenna, MIMO, power amplifier, nonlinear distortion, electrothermal, thermal model.

Acknowledgment

I have received the help and company of many people during my doctoral study, and I here would like to recognize their invaluable assistance.

First, I would like to express sincere gratitude and appreciation to my main supervisor, Professor Christian Fager, for guidance, encouragement, and patience. Thank you for the trust and confidence you have shown in me, which helped me work to the best of my ability. Without your continuous and comprehensive support, I could not pursue my challenging project.

I would also like to extend my sincere thanks to my co-supervisor, Associate Professor Koen Buisman for ingenious advice and feedback on my research. Thank you for always being supportive and committed to my work.

I wish to express my appreciation to my examiner Professor Herbert Zirath. It is a great honor for me to be part of your inspiring research group.

I would like to thank NXP Semiconductor for hosting my eighteen-months industrial internship. In particular, I wish to thank Ir. Marcel Geurts for the productive collaboration and hospitality at NXP. I also wish to thank Ir. Martin Versleijen, my industrial supervisor, for the guidance and patience that cannot be underestimated. I am very grateful for everything you taught me.

I want to thank all the colleagues of the Microwave Electronics Laboratory for the supportive and friendly work environment. A special thanks go to Han Zhou, Sara Hesami, Jose-Ramon Perez-Cisneros, Roger Argaez Ramirez, Ahmed Adel Hassona, Sining An, Frida Olofsson, and Lise Aabel. I had spent many good times with you, both in and out of work. Thank you so much.

I have had the chance to enjoy the company of many friends from SILIKA project and NXP semiconductor company in these years. I wish to thank all of them for cheering me up and for their reliable friendship. Special thanks go to Artem Roev, Mohammad Hossein Moghaddam, Marzieh SalarRahimi, and Eduardo Vilela Pinto Dos Anjos for their valuable friendship. We had a wonderful time during our industrial secondment, which I will never forget.

I would also like to thank my friends, Madeleine and Carlo, with whom I have shared moments of happiness and fun, but also my challenges. Thank you so much for everything.

And finally, thank to Abolfazl, who has been by my side throughout these years, living every single minute of it, and without whom, I would not have proceeded to this stage.

This work is a part of the Silicon-based Ka-band massive MIMO antenna systems for new telecommunication services (SILIKA) project, funded by the European Union 2020 research and innovation program under the Marie Sklodowska Curie grant agreement No.721732. Part of the work has also been carried out in the GigaHertz Centre in a joint project financed by the Swedish Government Agency for Innovation Systems (VINNOVA), Chalmers, Ericsson, Keysight Technologies, Infineon, Saab, and UMS.

Parastoo
Göteborg, Dec 2021

List of Publications

This thesis is based on the following appended papers:

Paper [A]

P. Taghikhani, K. Buisman and C. Fager, "Hybrid Beamforming Transmitter Modeling for Millimeter-Wave MIMO Applications", Published in *IEEE Transactions on Microwave Theory and Techniques,* vol. 68, no. 11, pp. 4740-4752, Nov. 2020.

Paper [B]

A. Roev, **P. Taghikhani**, R. Maaskant, C. Fager and M. Ivashina, "A Wideband and Low-Loss Spatial Power Combining Module for mm-Wave High-Power Amplifiers", Published in *IEEE Access,* vol. 8, pp. 194858-194867, 2020.

Paper [C]

P. Taghikhani, K. Buisman, M. Versleijen, J. -R. Perez-Cisneros and C. Fager, "Temperature-dependent Characterization of Power Amplifiers Using an Efficient Electrothermal Analysis Technique", Accepted for publication in *IEEE Transactions on Microwave Theory and Techniques,* October, 2021.

Other related publications by the Author not included in this thesis:

[i] M. SalarRahimi, E. V. P. d. Anjos, **P. Taghikhani**, V. Volski, C. Fager, D. M. M. Schreurs , G. A. E. Vandenbosch, M. Geurts "A Cost-Efficient 28 GHz Integrated Antenna Array with Full Impedance Matrix Characterization for 5G NR, "*IEEE Antennas and Wireless Propagation Letters*, vol. 19, no. 4, pp. 666-670, April 2020.

[ii] H. V. Hünerli, M. Gavell, **P. Taghikhani** and C. Fager, "A Methodology for Analysis of mm-Wave Transmitter Linearization Trade-offs Under Spectrum Constraints", *2018 International Workshop on Integrated Nonlinear Microwave and Millimeter-wave Circuits (INMMIC)*, Brive La Gaillarde, 2018, pp. 1-3.

[iii] J. Yang, F. Fangfang and **P. Taghikhani**, "Half-height-pin Gap Waveguide Technology and its Applications in High Gain Planar Array Antennas at MillimeterWave Frequency", *IEICE Transactions on Communications*, vol. 101, no. 2, pp. 285-292, 2018.

[iv] **P. Taghikhani**, J. Yang and A. Vosoogh "High gain V-band planar array antenna using half-height pin gap waveguide,", *2017 11th European Conference on Antennas and Propagation (EUCAP)*, Paris, 2017, pp. 2758-2761.

Thesis

[v] **P. Taghikhani**, "Active Transmitter Antenna Array Modeling for MIMO Applications," Thesis for the Degree of Licentiate of Engineering, MC2 Department, Chalmers University of Technology, Gothenburg, 2020.

Some of the work presented in this thesis, such as text, figures, and tables may partly or fully be reused from [v], which is a part of the author's doctoral studies.

Acronyms

AMAM	Amplitude Modulation to Amplitude Modulation
AMPM	Amplitude Modulation to Phase Modulation
CAD	Computer Aided Design
CW	Continous Wave
DPD	Digital Predistortion
DUT	Device Under Test
EM	Electromagnetic
EVM	Error Vector Magnitude
FIR	Finite Impulse Response
IC	Integrated Circuit
LTE	Long Term Evolution
MIMO	Multiple-Input Multiple-Output
mmWave	Millimeter Wave
OTA	Over The Air
PA	Power Amplifier
PAPR	Peak to Average Power Ratio
PHD	Poly Harmonic Distortion
RF	Radio Frequency
RMS	Root Mean Squared Error
RX	Receiver

TX	Transmitter
VNA	Vector Network Analyzer

Contents

Chapter 1

Introduction

1.1 Background

The demand for faster and more reliable communications is growing dramatically in society and in organizations. It is anticipated that there will be around 8 billion mobile subscribers at the end of 2025, of which 2.6 billion use the 5th Generation (5G) radio network [1], see Fig. 1.1. The available bandwidth at sub-6 GHz, the primary spectrum for 5G, is not enough to fulfill the anticipated capacity demands. Therefore, vast available bandwidth at mmWave bands, frequencies between 24 and 71 GHz, is opened up for 5G communications [1–5]. The advantages of using mmWave frequencies come at the cost of higher propagation loss. However, the mmWave loss can be partly compensated by using high-gain antennas or large-scale antenna arrays. The use of large antenna arrays is beneficial for increasing signal strength toward the user, overcoming path loss, and higher capacity of MIMO communication [6–8]. In particular, antenna arrays provide beamforming flexibility, which is also highly favorable for massive Multiple Input Multiple Output (MIMO) mobile communications.

The most flexibility of beamforming is achieved by using an independent TX/RX chain for each antenna. However, this configuration, referred to as digital beamforming, faces challenges from complexity and high power consumption, particularly at mmWave frequencies where the antenna separation is small, and at large signal bandwidths. Therefore, hybrid digital and analog architectures are developed as a practical solution for mmWave MIMO systems. Each of the RF chains in the hybrid architecture is, in such systems, connected to a subarray of antennas using an analog beamforming network [6, 7, 9–11]. For transmitters in both types of these architectures, an active antenna array is employed in which each antenna element is driven by a power amplifier (PA). Fig. 1.2(a) shows the transmitter configuration serving an active antenna array.

Transmitters in MIMO systems face challenges associated with linearity, efficiency, and heat dissipation [12–15]. Therefore, it is of paramount importance to understand and predict their behavior before implementation. Particularly, complex multi-branch transmitters require efficient yet accurate techniques to estimate their behavior.

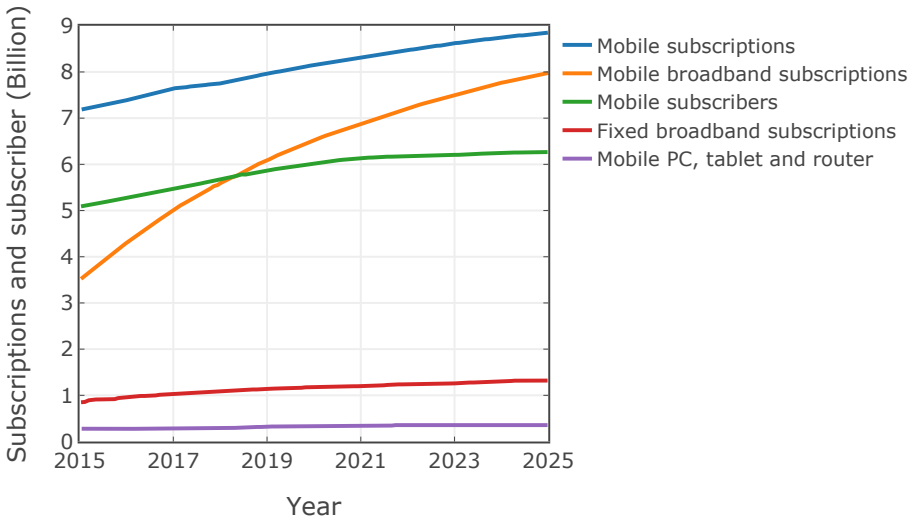

Figure 1.1: Estimated number of fixed and mobile subscriptions and subscribers (billions) until 2025 [1].

1.2 Transmitter Modeling

The performance of an active antenna transmitter depends on the electromagnetic (EM) behavior of the antenna array, circuit performance of PAs, and the effects of temperature variations and self-heating. Dedicated EM, circuit, and thermal computer-aided design (CAD) tools are available to design and evaluate transmitters sub-systems such as PA and antenna array individually. However, at the transmitter level, applying joint circuit and EM simulation using CADs is a complicated and time-consuming task for analyzing large active antenna arrays [12, 13, 18]. Also, for the electrothermal analysis of PAs and transmitter circuits, using circuit and thermal solvers in a coupled way is highly time-consuming and inefficient [19–21]. Therefore, such a detailed simulation is not suitable for evaluating transmitter behavior under realistic operating conditions. In these occasions, an analysis approach based on behavioral models of PAs and the antenna array is the key to a fast and accurate prediction of an active antenna transmitter performance characteristics.

Behavioral models are a mathematical description of a sub-system's specific input and output relationships that are important and relevant for the analysis at the transmitter level. These models can be obtained from CAD tools or measurements and must present the behaviors of the sub-systems adequately. Fig. 1.2(b) shows a conceptual representation of the joint analysis related to active antenna transmitters. The analysis framework can be made using well-defined behavioral models of the transmitter sub-systems.

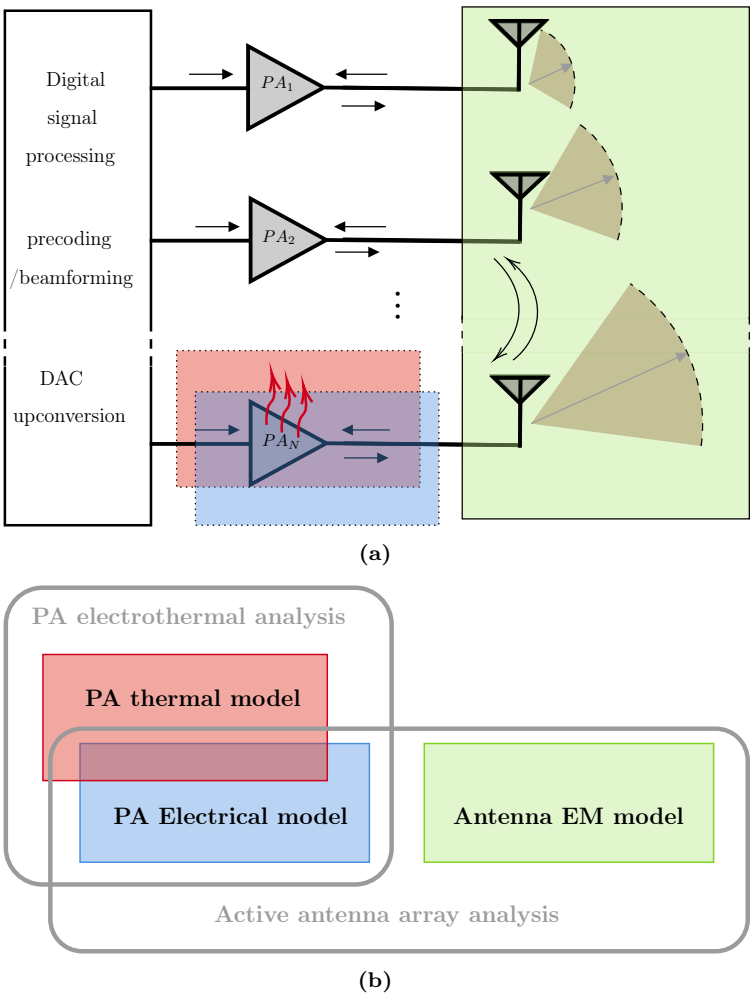

Figure 1.2: Illustration of an analysis framework for active antenna transmitter; a) Configuration of the transmitter; b) Analysis framework and modeling approaches.

1.2.1 Active Antenna Transmitter Modeling

Fig.1.3 shows an example of a mmWave integrated active antenna array system for 5G application developed by Ericsson and IBM [16, 17]. Each RF path is connected to an antenna element using multi-branch beamforming integrated circuits (ICs) placed at the backside of this configuration. Due to the small wavelength and physical dimensions at mmWave frequencies and the high level of integration, isolators cannot be used to eliminate mismatches and unwanted interactions between PAs and antennas, see Fig. 1.3. Therefore, PAs are susceptible to the waves incoming from the antenna array due to mismatch and mutual coupling between antenna elements. In this condition, including interactions between the antenna array and PAs become a significant aspect in analyzing an active antenna transmitter and individual characterization of PAs [13, 22, 23].

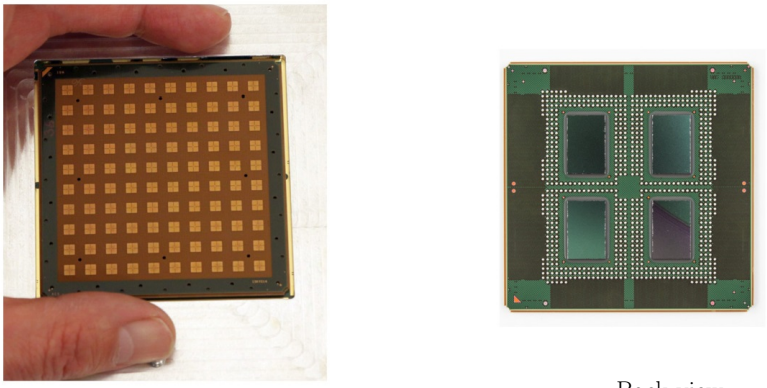

Front view Back view

Figure 1.3: 28 GHz active antenna array for mmWave 5G communication systems. The antenna array dimension is 70×70 mm and beamforming ICs are placed at the backside of the module [16,17].

Therefore, for an efficient analysis of active antenna transmitters, both the analysis framework and incorporated behavioral models of PA and antenna array should account for the unwanted interaction between them. Furthermore, it is essential to consider the radiated field characteristics of the antenna array in the analysis framework and as the transmitter output. Such an analysis framework can define valuable design guides for PA, antenna array, and transmitter configuration.

1.2.2 Electrothermal Modeling of PAs

Heat dissipation and challenges related to thermal issues impact reliability and performance of transmitters significantly. Particularly, in mmWave active antenna transmitters, high level of integration, small physical separation between antenna elements, and the implementation of low-efficiency PAs increase the heat dissipation challenges [24, 25].

In transmitters, PAs dominate heat dissipation and power consumption. Apart from thermal management and reliability issues, the performance of PAs are temperature-dependent. In particular, challenges associated with signal linearity are highly influenced by the electrothermal behavior of PAs under dynamic operating conditions. For this reason, an electrothermal analysis of PAs is required to predict the static and dynamic performance of transmitters accurately. The electrothermal analysis can be done by coupling a thermal solver with an electrical solver in an iterative way, see Fig. 1.4. In this approach, the device temperature and dissipated power are exchanged between two solvers until a consistent solution is found. However, such an approach is often time-consuming and computationally expensive. Therefore, it is crucial to develop efficient methods for the electrothermal analysis of PAs. The efficient analysis approach can be utilized for optimum thermally-aware design and evaluation of PAs. Furthermore, an efficient electrothermal analysis approach can be incorporated in

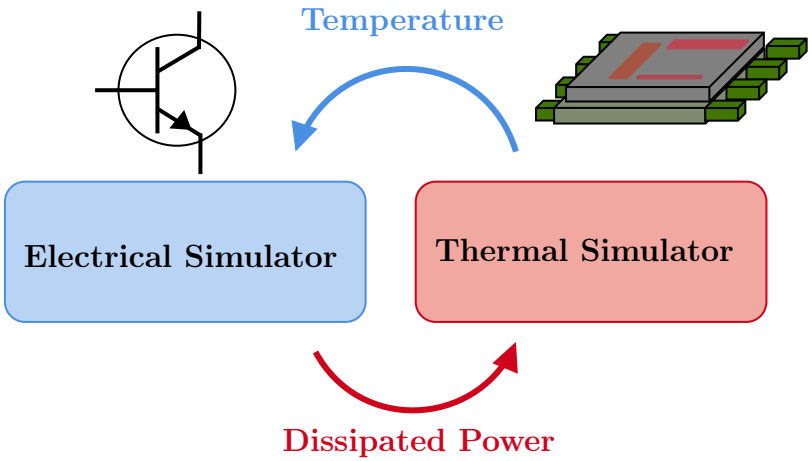

Figure 1.4: Coupled electrothermal simulation using thermal and electrical simulators.

the active antenna transmitter analysis framework for thermally-aware prediction of transmitters [26, 27]. Such an analysis approach can be applied at the early design stages of the transmitter to extract guidelines for co-design of the antenna array and PAs considering EM, circuit, thermal transmitter performance.

1.3 Thesis Contribution

This thesis attempts to develop efficient methods for analyzing active antenna transmitters by applying joint circuit, EM, and thermal modeling approaches. The initial focus has been on developing an efficient method for active antenna transmitter modeling that addresses the joint PA and antenna effects on the transmitter performance, such as radiation pattern and in-beam signal nonlinear distortion. This work was followed up in Paper [A]. The active antenna transmitter model is applicable for both digital and hybrid beamforming transmitters and is applied to a hybrid beamforming architecture and beam steering scenarios. Unlike the previously proposed PA models for multi-antenna transmitter analysis, the proposed PA model is not limited to small levels of mismatches and is equally accurate for any mismatches level. We have performed experiments with a mmWave hybrid beamforming subarray module to validate the proposed analysis. The subarray module includes a typical beamforming IC and a subarray antenna. The experimental validation results are therefore demonstrated for a beam steering scenario. The transmitter model is then exploited in a simulation study to predict the linearity in different array configurations.

The load-pull-based PA models introduced in Paper [A] are used to investigate the interaction between PAs in a spatial power combiner. In Paper [B], we investigate the critical coupling effects on the active performance of a multi-channel spatial power combining module. The coupling between combiner channels can create non-optimum loading conditions at the output of the connected PAs and deteriorate combining

performance. Such situations happen if the ports excitations become non-uniform due to non-identical PA behaviors.

The efficient modeling and analysis approach for transmitters is extended to include the effect of heat dissipation in PA behavior and consequently transmitter performance. In Paper [C], we propose computationally-efficient methods for thermal modeling and electrothermal analysis of PAs, including thermal model and equivalent thermal network extraction, using finite element method (FEM) thermal simulation data and nonlinear fitting algorithms. These form the basis for the development of efficient electrothermal analysis methodologies for the temperature-dependent characterization of PAs. The static and dynamic performance of a PA Device Under Test (DUT) is experimentally evaluated.

The proposed modeling approaches provide efficient tools for correctly predicting the joint circuit, EM, and thermal behavior of active antenna transmitters.

1.4 Thesis Outline

This thesis is organized into six chapters. Following this introduction, Chapter 2 describes the essential PA characteristics and a variety of behavioral models. First, a brief introduction to PA fundamental nonlinear characteristics is given. Then, the PA models for transmitters with isolated and coupled paths are described. Finally, temperature-dependent PA models are introduced. Chapter 3 explains the proposed active antenna transmitter modeling algorithm and experimental validation results related to a hybrid beamforming subarray module. It will explain the effect of mutual coupling in antenna array theory which is crucial in analyzing active antenna transmitters. This chapter also covers the joint PA and combiner performance evaluation. Chapter 4 describes the two proposed methodologies for the efficient electrothermal analysis of PAs. Furthermore, it covers the concepts of thermal impedance, thermal model extraction, and equivalent thermal network. Finally, Chapter 5 provides the conclusions of the thesis, primary contributions, and future work.

Chapter 2

Power Amplifier Modeling

Power amplifiers play an essential role in wireless communication systems. The PA principal role is to amplify an RF signal to a power level suitable for transmission. However, PAs are significant contributors to the power consumption, signal distortion, heat dissipation, and efficiency of transmitters [28]. The high power operating regime and inherent nonlinearity of PAs affect the signal quality of transmitters adversely. Therefore, to analyze the performance of active antenna transmitters, it is critical to characterize and model PA behavior properly.

This chapter presents a brief introduction to the PA nonlinear characteristics, modeling structures, and model identification. Dual input PA models are introduced for modeling transmitters of MIMO communication systems. Temperature-dependent models are introduced for electrothermal characterization of PAs. The chapter ends with a summary.

2.1 AM/AM and AM/PM Characteristics

Power amplifiers are commonly characterized by their gain and phase-shift as a function of input or output power. These characteristics are called amplitude modulation to amplitude modulation (AM/AM) and amplitude modulation to phase modulation (AM/PM). The shape of the AM/AM and AM/PM curves provide insightful information about the PA nonlinearities [29]. Typically, AM/AM and AM/PM characteristics are obtained when a PA is excited with a single tone signal. In this case, the AM/AM and AM/PM curves are a one-to-one mapping. Under modulated signal excitation, the instantaneous gain and output phase versus instantaneous input power is plotted to show dynamic AM/AM and AM/PM characteristics. Therefore, these curves show dispersive data. The dispersion gives a qualitative indication of the PA memory effects. Fig. 2.1 represents the measured AM/AM and AM/PM of a class AB PA which is operated at 2 GHz [30].

The memory effect is an inherent characteristic of a power amplifier which appears

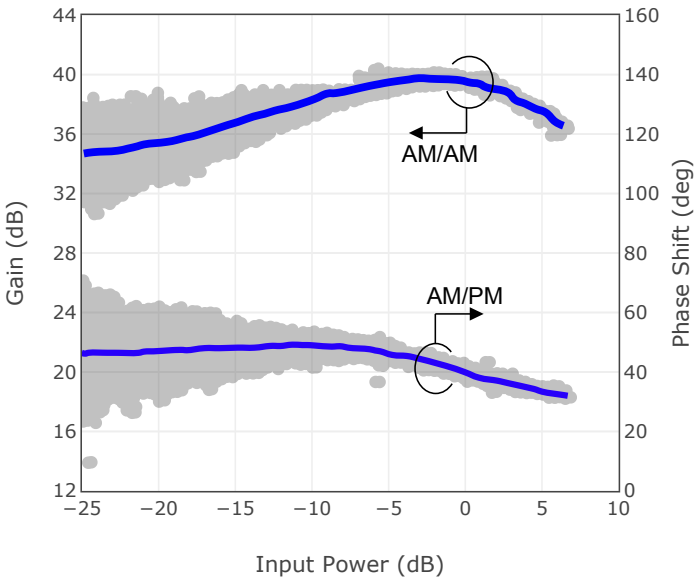

Figure 2.1: An example of PA AM/AM and AM/PM characteristics. Dispersive gray dots show dynamic PA behavior under modulated input signal with 10 MHz bandwidth [30].

due to the PA intrinsic and extrinsic parasitic elements, reactive elements in matching network, and the energy storage nature of transistor junctions. Self-heating is also another critical source of memory effects in PAs [31]. The memory effect of the PA can be ignored when the input signal is a single tone or a modulated signal with a narrow bandwidth. This simplification is valid if the amplifier behavior is constant/flat over the input signal's bandwidth. In this case, AM/AM and AM/PM conversion of PA at the carrier frequency characterize the PA within the signal bandwidth [29].

2.2 PA Behavioral modeling

A PA behavioral model characterizes the PA behavior such as output power, efficiency, etc., as a function of different input variables [32]. Unlike PA physical models, which are more suited to circuit-level simulation, behavioral models are based on the mathematical dependence of specific input and output characteristics and are aimed at the analysis at the transmitter level. Creating a behavioral model requires defining the model structure, collecting a set of input and output data, and determining model coefficients. The model applicability depends on the model structure. An example could be static and dynamic models developed to predict single tone or wideband input signals. A variety of PA behavioral models have been proposed so far for different applications. PA models can be categorized as single input models and load-dependent models. The latter has been proposed for MIMO systems where the

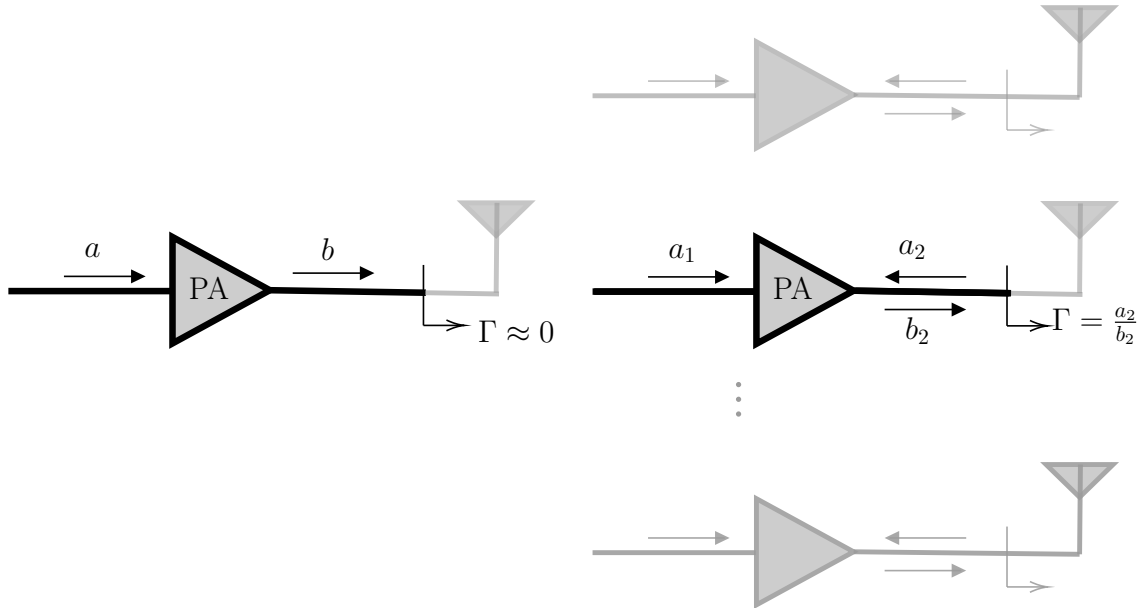

Figure 2.2: Block diagram of a) single path, b) multi path transmitter for the purpose of PA modeling

PA output is subject to signals from other transmit branches. The PA behavioral models are extended to temperature-dependent models when the problem of heat dissipation and thermal issues needs to be accurately considered.

2.2.1 Single Input PA Model

Fig. 2.2(a) shows the block diagram of a single chain transmitter for PA behavioral modeling. It is assumed that there is no reflected wave at the PA output. The suitable behavioral model, following the complex baseband envelope descriptions [33], is presented as

$$b(n) = f(a(n)), \tag{2.1}$$

where $b(n)$ is the PA output power[1] wave and described as a function of the power wave incident to the PA input $a(n)$. The function f, characterizes PA nonlinear behavior. Moreover, for simplicity in mathematical representation, the dependency of $b(n)$ to current and past samples of input waves, i.e. $f(a(n-1), a(n-2), ...)$ is not shown here and throughout the thesis. Such a model is also valid for the multi-antenna transmitters if the RF paths are isolated.

A variety of functions have been proposed for the single input PA model structure [35–38]. Volterra series model and the pruned version of it i.e. polynomial, memory

[1]Power wave terms are introduced by D. M. Pozar [34], Chapter 4.

polynomial [37], generalized memory polynomial [38] are among the most popular PA behavioral models. The static polynomial model is represented as

$$b(n) = \sum_{p=0}^{(P-1)/2} \alpha_p a(n)|a(n)|^{2p}, \tag{2.2}$$

where $b(n)$ and $a(n)$ are the baseband complex envelop of PA input and output power waves. α_p are the complex model coefficients and P is the nonlinear model order. Only odd-order terms are present since the distortion produced by the even-order components are far from the carrier frequency and do not contribute to the PA output within its intended bandwidth [39].

The memory polynomial model for characterizing PAs with dynamic behavior is formulated as [37]

$$b(n) = \sum_{p=0}^{(P-1)/2} \sum_{m=0}^{M} \alpha_m^p a(n-m)|a(n-m)|^{2p}, \tag{2.3}$$

where α_m^p are the model complex coefficients. P and M represent the nonlinear model order and memory depth, respectively.

2.2.2 Dual Input PA Model

The transmitter in MIMO systems has several RF transmit chains, including individual PAs to drive an antenna array. Modern transmitters avoid bulky isolators between PA and antenna due to the high integration and lack of spacing. Thus, PAs become susceptible to the waves leaking from other branches. Especially, mismatch and mutual coupling in the antenna array create a variable active load, Γ_i, at the output of each PA, as will be described in Sec. 3.1.2. Variations in output impedance affect the linear and nonlinear behavior of each PA. The conventional PA model cannot describe their behavior in these cases. Fig. 2.2(b) presents the block diagram for modeling PA in a MIMO system. The PA output in the k-th branch is described as

$$b_2(n) = f(a_1(n), a_2(n)), \tag{2.4}$$

where $b_2(n)$ is the PA output and described as a function of the two incident power waves, i.e $a_1(n), a_2(n)$ in the k-th transmit path. $f(.)$ is a nonlinear mathematical function that describes the effects of amplification as well as the effects of PA output load variation (Γ_i). Equation (2.4) is referred to as a dual input PA model.

Until now several dual input PA models have been introduced [22, 23, 40–49]. In [43, 46] a dynamic dual-input PA model is developed which characterizes PA under mismatch at the input and output. Zakka in [49] proposed a memoryless dual input PA model based on Poly-Harmonic Distortion (PHD) [48] modeling approach to use

in a macro transmitter modeling. Fager, et al. [22] proposed a memory polynomial dual-input model which is suitable for wideband signals. As an example, the structure of the memory polynomial dual-input model proposed by [22] is presented here. This model is developed based on expanding a PHD model with memory effects.

$$
\begin{aligned}
b_2(n) = & \underbrace{\sum_{m_1=0}^{M} \sum_{p_1=1}^{P_1} \alpha_{m_1}^{p_1} |a_1(n-m_1)|^{2p_1-1}}_{S_{21}(|a_1|)} a_1(n-m_1) + \\
& \underbrace{\sum_{m_2=0}^{M_2} \sum_{m_1=0}^{M_1} \sum_{p_2=1}^{P_2} \beta_{m_1,m_2}^{p_2} |a_1(n-m_1)|^{2(p_2-1)}}_{S_{22}(|a_1|)} a_2(n-m_2) + \\
& \underbrace{\sum_{m_2=0}^{M_2} \sum_{m_1=0}^{M_1} \sum_{p_2=2}^{P_2} \gamma_{m_1,m_2}^{p_2} a_1^2(n-m_1) |a_1(n-m_1)|^{2(p_2-2)}}_{T_{22}(a_1)} a_2^*(n-m_2),
\end{aligned}
\tag{2.5}
$$

where (P_1, P_2) and (M_1, M_2) are the nonlinear model orders and memory depth, respectively. Similar to a classical S-parameters definition, the term $S_{21}(|a_1|)$ maps the incident wave a_1 to the wave b_2. Likewise, $S_{22}(|a_1|)$ maps a_2 to b_2 wave. S_{21} and S_{22} depends on the amplitude of the input wave. $T_{22}(a_1)$ is a term that depends on amplitude and phase of input wave and map the conjugate of a_2 wave to b_2. The two last parts of (2.5) describe PA nonlinear behavior due to the effect of waves coming from other branches and $S_{21}(|a_1|)$ is showing the large signal gain of the PA.

Using interpolation functions

Models presented so far rely on specific mathematical representations based on knowledge of PA behavior. In many practical applications, the PA nonlinear characteristics are achieved experimentally. Therefore, an adequate mathematical function may not be easily found. An alternative model, which is also helpful for computer simulation, can be a tabular representation of experimental data [29, 50, 51].

An interpolation function can also be used to map input-output data relationships. Computing software nowadays comes with built-in interpolation functions such as piecewise linear. Thus, an interpolation function can approximate the PA behavior without being constrained by a polynomial model as described above. Piecewise interpolation function, as an example, have the advantage of being equally accurate for all points within the measured data range. Therefore, it can characterize PA behavior for large mismatches with reasonable accuracy. Paper [A] used a piecewise linear interpolation function to characterize the PA static nonlinear behavior versus different output loading conditions.

Including the memory effect in the interpolation model is not trivial. One approach can be to develop an interpolation function that treat the delayed signal as a new variable. Therefore, the model relates the instantaneous complex gain of PA to the instantaneous inputs and M preceding samples as M new variables (memory depth).

2.2.3 Temperature-dependent Model

The introduced behavioral models in Sec. 2.2.1 and 2.2.2 describe the PA output as a function of its input and reflected waves at the output. It is well known that the PA performance also depends on its operating temperature. Behavioral models with temperature dependency are suitable for the temperature-aware and electrothermal analysis of transmitters. Therefore, the single input model structure in (2.1) is modified as

$$b(n) = f_{th}(a(n), T(n)) \tag{2.6}$$

where $T(n)$ is the PA effective temperature. Similarly, the structure of dual input model in (2.4) is adapted to a temperature-dependent PA model as

$$b_2(n) = f_{th}(a_1(n), a_2(n), T(n)) \tag{2.7}$$

The function $f_{th}(.)$, characterizes PA nonlinear and temperature-dependent behavior. The introduced static and memory polynomial models in (2.2), (2.3) and (2.5) can then be transformed to temperature-dependent models by modifying the model coefficients [26, 27, 52]. The model in (2.2) is modified as

$$b(n) = \sum_{p=0}^{(P-1)/2} \alpha_p(T(n))a(n)|a(n)|^{2p} \tag{2.8}$$

where $\alpha_p(T(n))$ is the temperature-dependent model coefficient. Equivalently, the model coefficient in (2.5) and (2.3) are rewritten as $\alpha_{m_1}^{p_1}(T(n)), \beta_{m_1,m_2}^{p_1}(T(n))$ and $\gamma_{m_1,m_2}^{p_1}(T(n))$ to include temperature dependency.

For electrothermal analysis of PAs and temperature-aware transmitter performance prediction, temperature-dependent models of dissipated power are required. Following an approach similar to the single input PA modeling, the temperature dependence of the PA power dissipation, P_{diss}, is modeled by a polynomial expression as

$$\begin{aligned} P_{diss}(n) = P_{dc}(n) + P_{in}(n) - P_{out}(n) &= f_p(a(n), T(n)) \\ &= \sum_{p_d=0}^{P_d} \xi_{p_d}(T(n))|a(n)|^{p_d} \end{aligned} \tag{2.9}$$

where $P_{in}(n)$ and $P_{out}(n)$ represent the power of the input, $a(n)$, and output waves, $b(n)$, respectively. $P_{dc}(n)$ is the supply dc power. In contrast to RF behavioral

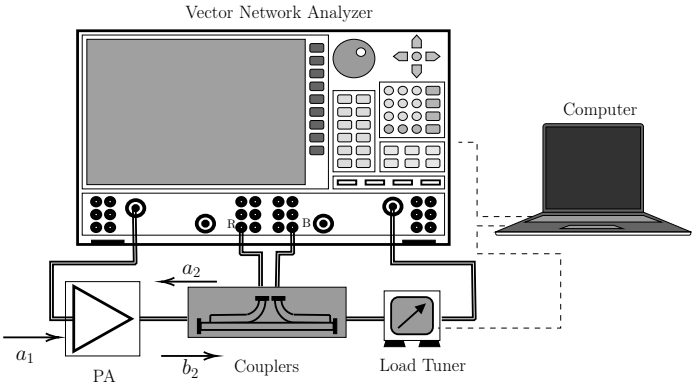

Figure 2.3: Block diagram of a conventional load-pull measurement setup.

models, this model includes all nonlinear orders, including zero-order quiescent power dissipation. $\xi_{p_d}(T(n))$ are real-valued model coefficients leading to a real value for dissipated power.

The PA thermal response is typically much slower than the RF signal response. Therefore, the required data for determining temperature-dependent model coefficients can be acquired by repeating pulsed RF measurements or circuit simulations at different ambient temperatures.

2.2.4 Model Identification

Once the model structure is specified, a set of measured or simulated data representing the PA output versus known inputs is required to identify the model. The measured or simulated data is used to obtain the model coefficients or to develop an interpolation function. For single-input models, data collection for model identification is relatively straight forward. However, for dual-input models, load-pull is required to emulate a_2 waves. As it is described in Sec. 2.2.3, data for temperature-dependent model identification coefficients can be acquired by repeating measurements or circuit simulations at different ambient temperatures.

Load-Pull Measurements

In conventional load-pull experiments, a passive tuner changes the output load impedance of the PA. The reflected wave back to the PA output, a_2, can be collected using directional couplers. Active load-pull instead uses an adjusted signal to be injected into the PA output [53, 54]. The model coefficients or interpolation function can be specified by measuring the incident and reflected waves at the PA ports.

In Paper [A], we performed passive load-pull measurements to develop the static interpolation function of the PA integrated into a beamforming IC. Fig. 2.3 shows the block diagram of the load-pull measurement setup. a_1 is a single tone continuous wave (CW) signal at 29 GHz frequency. a_2 and b_2 waves at the interface of the DUT

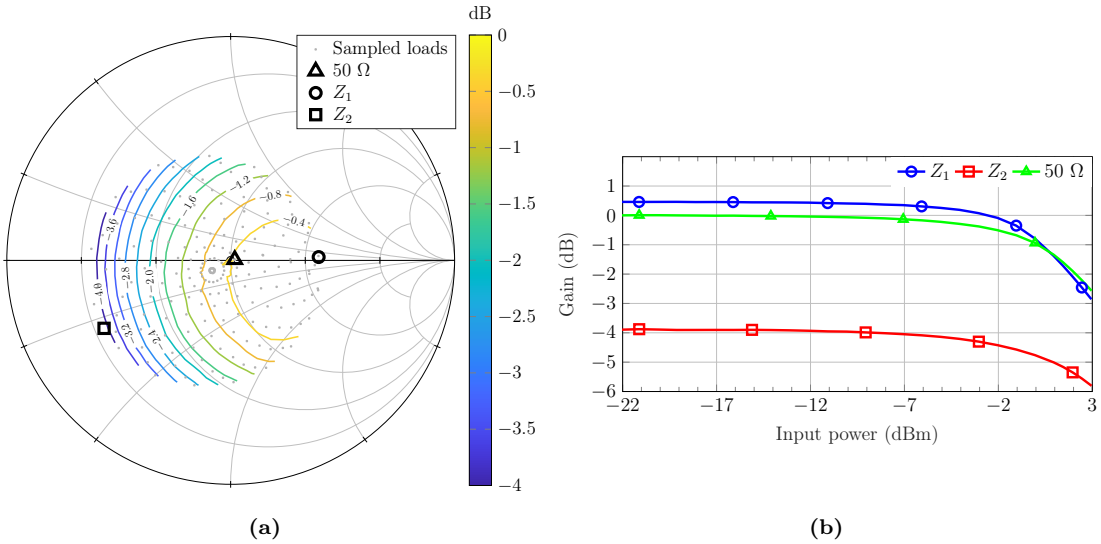

(a) **(b)**

Figure 2.4: a) Normalized delivered output power contours from load-pull measurement at 29 GHz. Markers are $Z_1 = 115 + j4$, $Z_2 = 11 - j12$ and 50Ω. Gray points indicate loads used during load-pull characterization, b) Normalized AM/AM for the different marked loads Z_1, Z_2 and 50 Ω. The results are normalized to the small signal measurements with a 50 Ω load.

are measured for each level of input power and specified tuner load. Therefore, the PA's AM/AM and AM/PM characteristics have been measured for all specified tuner loads.

Fig. 2.4(a) shows the normalized delivered output power contours that are obtained from the interpolated load-pull measurement data. Fig. 2.4(b) presents AM/AM plots for three different tuner loads, i.e. $Z_1 = 115 + j4$, $Z_2 = 11 - j12$ and 50 Ω. Plots are normalized to the gain values in the linear working region for the 50 Ω loading. The behavior and absolute levels of the AM/AM plots change with varying loading. Similar behavior is observed for AM/PM curves. Detailed information about the measurement scenario can be found in Paper [A].

Least Square Estimator

A least-square estimator finds the coefficients of the models which are linear in coefficients e.g. (2.2), (2.3), (2.5), (2.8) and (2.9) [55]. A linear-in coefficient PA model can typically be described as the summation of weighted (model coefficients) basis functions. For N number of PA input and output measured samples, the model can be written as

$$\mathbf{b} = \mathbf{H}(\mathbf{a})\boldsymbol{c}, \tag{2.10}$$

where $\mathbf{b}$ is a column vector containing the N measured samples of the PA output i.e. $\mathbf{b} = [b(1)..., b(N-1), b(N)]^T$. $\boldsymbol{c}$ is a column vector of the model coefficients. $\mathbf{H}(\mathbf{a})$ is

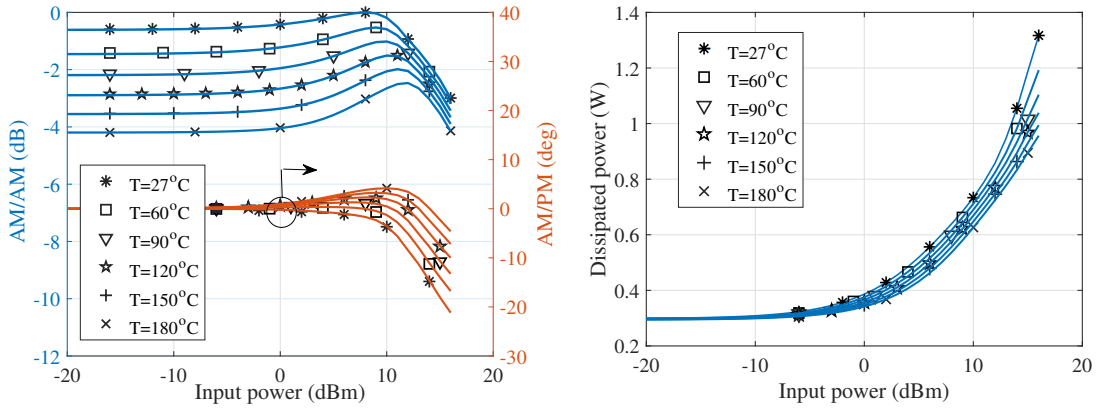

(a) (b)

Figure 2.5: Simulated (marker lines) and modeled (solid lines) PA DUT characteristics at six different temperatures: (a) gain variation / AM/AM and phase variation / AM/PM, (b) dissipated power (P_{diss}). AM/AM graphs are normalized to the PA maximum gain at 27°C ambient temperature

a matrix containing the evaluated nonlinear model basis functions based on known input samples, i.e. $a(n)$. For the dual input models, a set of $a_1(n)$ and $a_2(n)$ are used to evaluate the model basis functions. For the model in (2.9), $\mathbf{b}$ is the N measured or simulated samples of the PA dissipated power.

The least-square estimate of the model coefficients can be identified as

$$\hat{\boldsymbol{c}} = (\mathbf{H}^T\mathbf{H})^{-1}\mathbf{H}^T\mathbf{b}. \tag{2.11}$$

As described earlier, in Paper [A] we applied the measured data directly to develop the interpolation function. However, it is possible to map the measured data to a memoryless dual input polynomial model using the least square technique [47]. In Paper [C], we used a least square estimator to find temperature-dependent coefficients of (2.8) and (2.9).

Thermal Model Identification

In Paper [C], we used temperature-dependent behavioral nonlinear models for the electrothermal analysis of a PA device under test (DUT). The data were obtained by performing circuit simulations at different ambient temperatures. Then, the PA performance was mapped to the models in (2.6) and (2.9) using least square estimator. Fig. 2.5 presents the temperature-dependent AM/AM, AM/PM, and dissipated power of the PA DUT in Paper [C]. As it can be seen, there is a good agreement between the modeled and simulated results. The temperature-dependent behavioral models are used in an electrothermal analysis framework where the PA thermal model calculates the temperature, and PA behavioral models evaluate PA output and dissipated power. The temperature and dissipated power exchanged between models to accurately

take into account temperature variations on PA performance. The details about model-based electrothermal analysis are given in Chapter. 4.

2.3 Summary

Accurate prediction of PA performance requires considering temperature variations in behavioral modeling. At the same time, in MIMO transmitters, PAs are subject to waves coming from other branches. Therefore, developing new PA behavioral models suitable for transmitters in MIMO systems is of major interest. The use of a proper PA model is crucial for the correct analysis of the active antenna transmitter.

In this chapter, different PA behavioral modeling are reviewed. First, the PA nonlinear characteristics are described to the reader. The PA modeling is categorized into single input and dual input models for application in the active antenna transmitter modeling. The application of an interpolation function for PA modeling is introduced as an option to the typical polynomial-based models. Temperature-dependent models for PA analysis and system-level simulations of transmitters are introduced. Finally, the model identification method and the corresponding experimental characterization method are discussed.

Chapter 3

Active Antenna Transmitter Modeling

MIMO transmitters, in both digital- and hybrid beamforming architectures, are based on active antenna arrays. The analysis of MIMO transmitters, including several PAs and antennas, needs efficient methodologies. This chapter introduces the antenna array characteristics such as embedded element pattern and active impedance for arrays with significant mutual coupling. The importance of dedicated nonlinear modeling techniques for the analysis of active antenna transmitters is briefly described. Then, our proposed modeling approach for hybrid beamforming transmitters is introduced. The experimental results of a 29 GHz hybrid beamforming subarray module and succeeding simulation study of a large-scale hybrid beamforming transmitter are provided in the same section. Furthermore, this chapter describes the joint PA and combiner analysis and critical coupling effects on the performance of a spatial power combining module. The chapter finishes with a summary.

3.1 Antenna Array Characteristics

An antenna array is a set of antenna elements that work together and is designed such that the combined radiated signal has desired characteristics [56]. MIMO arrays can be thought of as an antenna array with advanced adaptive beamforming/signal processing, which exploits the complex surrounding environment to improve performance, e.g., in terms of channel capacity [56]. Therefore, an antenna array can have a wide range of architectures and capabilities. However, the underlying operating principle is shared among all configurations and applications.

The antenna elements and the excitation network are the two main parts of every antenna array. The excitation network is responsible for exciting the antenna elements such that the desired radiation characteristics are obtained. The array is called passive when a passive feeding network excites antenna elements from a common path. The

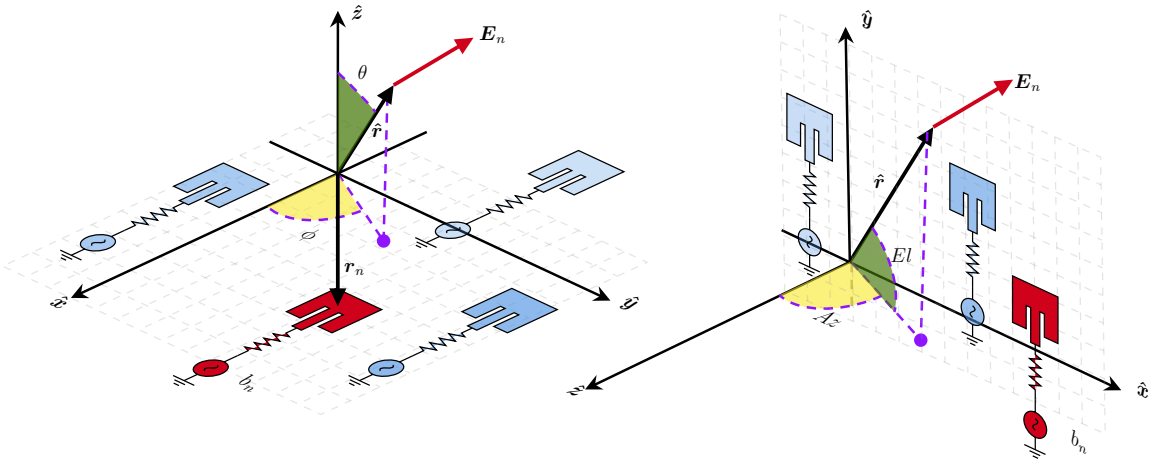

Figure 3.1: Illustration of a generic antenna array layout in spherical coordinate system (left) and Azimuth/Elevation coordinate system (right); each antenna element is located in position $\boldsymbol{r}_n$. The element radiated field is $\boldsymbol{E}_n$, and excitation waves are b_n.

active array is an array where each antenna element has a dedicated transmit or receive feeding path [56]. The active antenna array is more flexible and powerful, especially for beamforming purposes.

The radiation function, also defined as radiation pattern, represents the angular distribution of the radiated electric field of an antenna in the far-field region [57]. The radiation pattern is independent of the radial distance from the antenna in the far-field region. The radiation pattern of an antenna array including N antenna elements that are located at $\boldsymbol{r}_n = x_n\hat{\boldsymbol{x}} + y_n\hat{\boldsymbol{y}} + z_n\hat{\boldsymbol{z}}, n = 1, 2, ..., N$ is calculated as

$$\boldsymbol{E}(\hat{\boldsymbol{r}}) = \sum_{n=1}^{N} b_n \boldsymbol{E}_n(\hat{\boldsymbol{r}}), \quad \text{with} \quad \boldsymbol{E}_n(\hat{\boldsymbol{r}}) = \boldsymbol{E}_n^o(\hat{\boldsymbol{r}}) e^{jk_0 \boldsymbol{r}_n \cdot \hat{\boldsymbol{r}}}. \tag{3.1}$$

where $\hat{\boldsymbol{r}}(\theta, \phi) = \sin(\theta)\cos(\phi)\hat{\boldsymbol{x}} + \sin(\theta)\sin(\phi)\hat{\boldsymbol{y}} + \cos(\theta)\hat{\boldsymbol{z}}$ shows the vector of observation point at (θ, ϕ), see Fig. 3.1. $\boldsymbol{E}_n(\hat{r})$[1] is the element far-field radiation function[2] which is represented with respect to the array origin [56]. $\boldsymbol{E}_n^o(\hat{\boldsymbol{r}})$ is the element radiation pattern where the origin is on the antenna element itself, and assuming that the incident input power to the antenna element is unitary. $k_0 = 2\pi/\lambda$ is the wavenumber and $b_n = A_n e^{j\phi_n}$ is the complex value of the incident power wave to the n-th element with incident input power equal to $P_n^{inc} = \frac{1}{2}|b_n|^2$.

As it can be seen in Fig. 3.1, the (θ, ϕ) in spherical coordinate system can be

[1] $\boldsymbol{E} = \boldsymbol{E}_n(\hat{r})$ is the electric field vector which in Cartesian coordinate system can be written as $\boldsymbol{E} = E_x\hat{\boldsymbol{x}} + E_y\hat{\boldsymbol{y}} + E_z\hat{\boldsymbol{z}}$.

[2] Assuming the antenna elements are isolated. The accurate term is the embedded element radiation function which will be introduced in 3.1.2.

convert to azimuth and elevation coordinates (Az, El) angle by

$$\begin{aligned} \sin(El) &= \sin(\phi)\cos(\theta), \\ \tan(Az) &= \cos(\phi)\tan(\theta). \end{aligned} \tag{3.2}$$

Equation (3.1) shows that the array radiation pattern depends on the individual element radiation patterns, positions, and incident waves. The physical geometry of the array determines the first two quantities. However, the feeding network determines the incident power waves, e.g., the PA outputs in an active antenna transmitter.

3.1.1 Phased Array and Beam Steering

Phased arrays are antenna arrays that can provide electronic beam steering by applying phase-shifted excitations to the antenna elements. The beam steering allows the beam to be pointed toward specific users for quickly tracking or sweeping a large spatial sector [58]. However, to steer a highly directive beam toward a particular direction, it is vital to properly design the antenna element and array layout.

Fig. 3.2 shows the configuration of a linear and planar phased array with their corresponding steered beam. For an equally spaced linear array the required phase shift between element along the x-axis for steering the beam to θ_s can be obtained as [57]

$$\Delta\phi_x = kd\sin(\theta_s). \tag{3.3}$$

where d is the inter-element spacing. For an equally spaced planar array, the phase-shift between elements along the x- and y-axis to steer the antenna array beam toward (ϕ_s, θ_s) can be easily found as

$$\begin{aligned} \Delta\phi_x &= kd_x\sin(\theta_s)\cos(\phi_s), \\ \Delta\phi_y &= kd_y\sin(\theta_s)\sin(\phi_s). \end{aligned} \tag{3.4}$$

where d_x and d_y are the elements spacing along the x- and y-axis. Therefore, the excitation phase of element (n_x, n_y) with $n_x = 1, ..., N_x$ and $n_y = 1, ..., N_y$ is

$$\phi_{n_x,n_y} = -n_x\Delta\phi_x - n_y\Delta\phi_y. \tag{3.5}$$

3.1.2 Effect of Mutual Coupling

Every antenna element is typically characterized in isolation and away from surrounding bodies. In an array, the antenna element radiation characteristics are strongly affected by the neighboring antennas. The proximity between antenna elements can change the far-field radiation pattern enormously and also affect the impedance characteristics of each element significantly. These effects are referred to as mutual

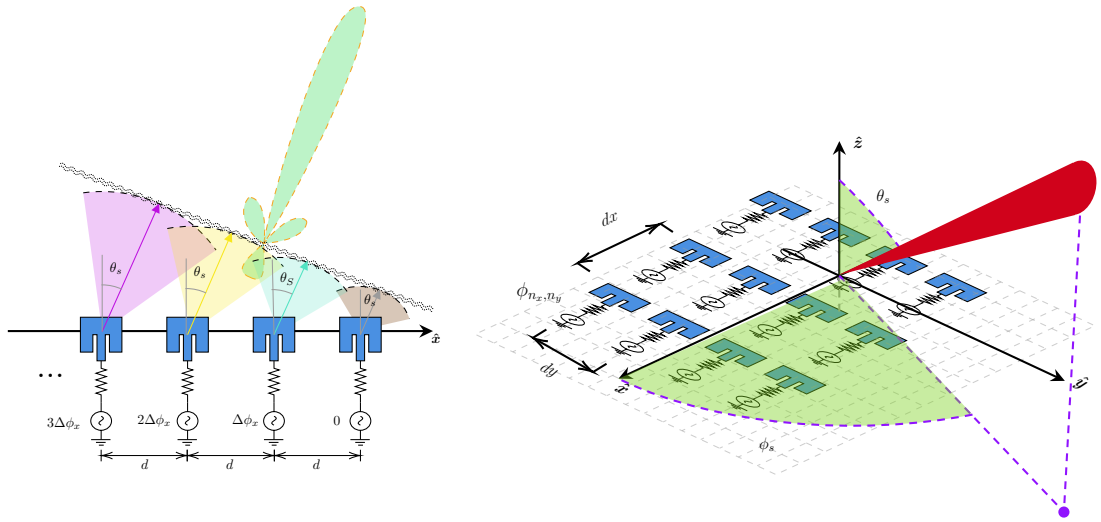

Figure 3.2: Illustration of a linear (left) and planar (right) phased array; $\Delta\phi_x$ is phase shift in linear array. N_x and N_y are the number of elements in planar array along x and y axis, respectively. ϕ_{n_x,n_y} is the excitation phase of corresponding element.

coupling and are often undesired in antenna arrays. For weakly coupled antennas, it is common to assume identical and isolated element radiation patterns. In a dense array, element radiation patterns can be very different from one another. Exciting one antenna element induces a current in the neighboring elements. The adjacent element thereby re-radiates and subsequently couples to the other antennas. Therefore, the total radiation pattern changes due to the radiation of the induced current. Also, the induced coupled current to the nearby antenna changes its port impedance. These effects are dependent on the antenna element excitations and the mutual coupling level. For an antenna array, the terms embedded element pattern and active impedance are defined to represent radiation pattern and port impedance in the presence of mutual coupling.

Embedded element pattern

The embedded element pattern is defined as the array radiation pattern when one element is excited, and the rest of the elements are passively terminated by a matched load, see Fig. 3.3 (b). Equation (3.1) can be then adopted based on embedded element patterns. In this representation, the mutual coupling effects are incorporated in the embedded element pattern definition and consequently into the antenna array radiation pattern [59]:

$$\boldsymbol{E}(\hat{\boldsymbol{r}}) = \sum_{n=1}^{N} b_n \boldsymbol{E}_n^{em}(\hat{\boldsymbol{r}}). \tag{3.6}$$

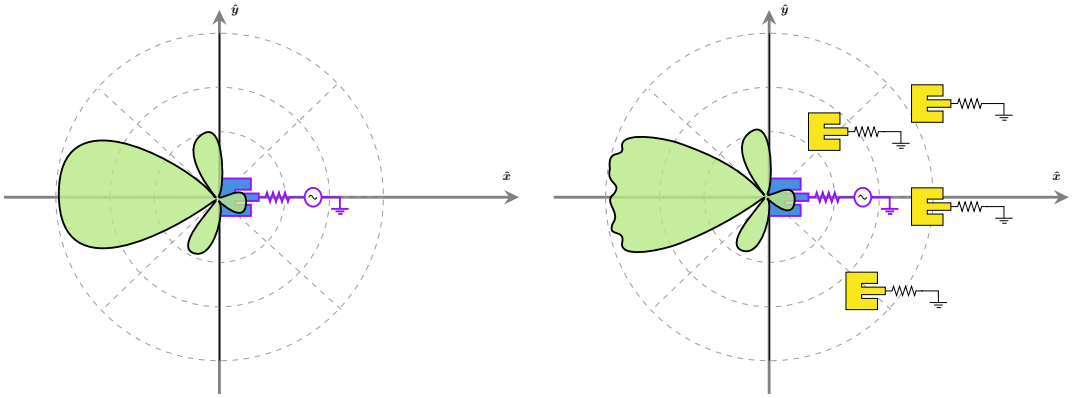

Figure 3.3: The antenna element radiation pattern. a) Isolated element pattern, b) Embedded element pattern; For a weakly coupled array, the isolated element pattern and embedded element pattern become similar.

In this formulation, it is assumed that embedded element radiation pattern is represented in respect to the antenna array origin. Otherwise, the $\boldsymbol{E}_n^{em}(\hat{\boldsymbol{r}})$ must be modified accordingly.

Active impedance

Each antenna element is characterized solely by its self-impedance. However, when an antenna element is placed in an array configuration its input impedance changes due to mutual coupling. The term active impedance refers to the input impedance of an element when all other array elements are active or excited. Consequently, the active impedance varies with array element excitations and mutual coupling level [59, 60]. Therefore, for a phased array it depends on the steering angle. In principle, the active impedance is different for each antenna element inside the array. For an array of N elements, the S-parameter is an $N \times N$ matrix which includes mismatch and mutual coupling of the array. $S_{n,m}$ are the elements of the array S-parameter matrix. Considering that the element excitations, b_n, are known, the i-th element active reflection coefficient is calculated as

$$\Gamma_i^{\text{act}} = \frac{\sum_{n=1}^{N} b_n S_{n,i}}{b_i}, \tag{3.7}$$

and accordingly, the active impedance with reference to Z_0 is

$$Z_i^{\text{act}} = Z_0 \frac{1 + \Gamma_i^{\text{act}}}{1 - \Gamma_i^{\text{act}}}. \tag{3.8}$$

$Z_{\text{act},i}$ is the antenna port impedance when all other antenna elements of the array are active. The active impedance often is calculated assuming that antenna element

excitations are independent of antenna array characteristics. However, in an integrated active antenna transmitter, antenna element excitations which are PA outputs, depend on signal back to the PAs due to the antenna array mismatch and mutual coupling, i.e., a_2, see Fig. 2.2.

The analysis of antenna arrays is a well-established topic in the antenna research area. Various EM simulation tools such as CST Microwave Studio and Ansys HFSS are available for highly accurate simulation of antenna and post-processing of antenna arrays. To analyze large-scale transmitter performance, a model which adequately represents antenna array behavior is applied.

3.2 Importance of Transmitter Modeling

The modeling of a transmitter helps to find a suitable description and understanding of its behavior. The model can then predict the transmitter's output for any specific input signal or understand observed measured results. Moreover, modeling is essential before implementing the hardware. Having adequate knowledge about the transmitter performance under realistic operating conditions can aid the modification or design of transmitter configuration and building blocks if needed to meet the required characteristics. The other advantage is that unwanted transmitter output, such as nonlinear distortion, can be predicted, and a proper compensation approach can be developed correspondingly. Furthermore, an accurate hardware-oriented transmitter model can be employed to evaluate different signal processing algorithms. Therefore, expensive and complicated measurement setups for such evaluations can be avoided, and the development speed can be improved.

An active transmitter antenna array consists of radiating antenna elements and PAs. They are designed and simulated individually using EM and circuit CAD tools such as Ansys HFSS, Keysight ADS, Cadence, etc. Antenna EM and active circuit CAD tools are developed for full-wave and circuit-level simulations. However, when performing analysis on the transmitter level, such a detailed simulation (in a co-simulation or combined EM/circuit form) is neither feasible nor logical for large active antenna transmitters. Furthermore, using these tools limit the investigation to the specific CAD capabilities and simulation results. For instance, EM and circuit CAD tools cannot deal with modulated signals efficiently. The works reported in [18, 61–63] proposed specific CAD-based approaches for the analysis of active antenna arrays that cannot be applied to modulated signal analysis and transmitters serving large antenna arrays.

3.3 Proposed Modeling Technique

The key to efficient and accurate assessment of active antenna transmitters is employing relevant behavioral models of transmitter building blocks, i.e., PAs and antenna array. Considering the interaction between the antenna array and PA is important in developing a framework for modeling active antenna transmitters.

The terminology used in this section assumes that all antennas and PAs work at the same center frequency. Digital signal processing units perform digital precoding, beamforming, and linearization, see Fig. 3.4. Precoding/beamforming weights are calculated based on the channel state information and by applying proper precoding techniques such as maximum ratio combining or zero-forcing [64, 65]. The transmitter modeling formulation maps the signal incident to the PA (the baseband complex envelop representation of incident power wave) to the radiated field signal, i.e., the active antenna transmitter output. The purpose of this modeling technique is to evaluate radiated signal characteristics. The signal radiated in the far-field provides valuable insight into transmitter performance in all spatial and user directions.

Fig. 3.4 shows the analysis framework for the active antenna transmitter with coupled antenna elements. The mutual coupling affects antenna element radiation patterns, antenna's active impedance, and PA outputs. The proper PA model for modeling the behavior of this transmitter is the dual-input model introduced in Sec. 2.2.2. In the k-th transmit path, the output of each PA is

$$b_2^{(k)}(n) = f_k(a_1^{(k)}(n), a_2^{(k)}(n)), \tag{3.9}$$

where $f_k(.)$ is k-th PA dual input behavioral model. $a_1^{(k)}(n)$ and $b_2^{(k)}(n)$ are the PA input and output signals, respectively. $a_2^{(k)}(n)$ is the incident signal to PA output due to antenna array mismatch and mutual coupling which is determined using the antenna array S-parameters, $\mathbf{S}_{\text{ant}}$, i.e.

$$\mathbf{a_2} = \mathbf{S}_{\text{ant}}\mathbf{b_2}, \tag{3.10}$$

where $\mathbf{a_2} = [a_2^{(1)}(n), a_2^{(2)}(n), ..., a_2^{(K)}(n)]^T$ and $\mathbf{b_2} = [b_2^{(1)}(n), b_2^{(2)}(n), ..., b_2^{(K)}(n)]^T$. This model structure is suitable for antenna S-parameters that are flat over the signal bandwidth. Finite impulse response (FIR) filters representing antenna mismatch and coupling can be used to model frequency-dependent antenna behavior, as in [66]. It is important to jointly solve (3.10) and (3.9) to find correct values for $b_2^{(k)}$. As described in Sec. 3.1.2, each antenna element radiated field is affected by mutual coupling. Therefore, the isolated element radiation pattern is not applicable and the embedded element pattern must be used. When the correct values of $b_2^{(k)}$ are found, the total radiation field is calculated as

$$\boldsymbol{E}(\hat{\boldsymbol{r}}, n) = \sum_{k=1}^{K} b_2^{(k)}(n)\boldsymbol{E}_k^{em}(\hat{\boldsymbol{r}}), \tag{3.11}$$

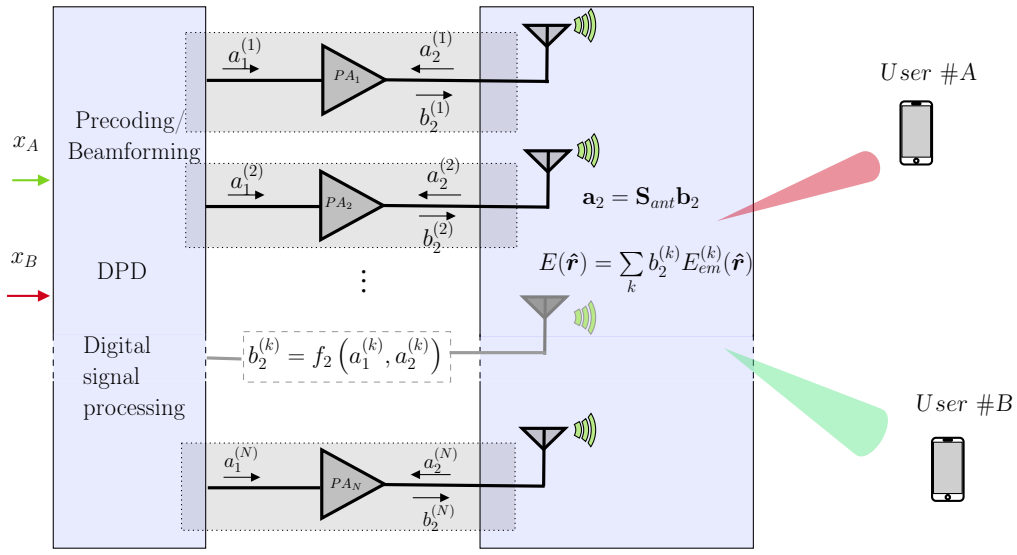

Figure 3.4: Digital beamforming MIMO transmitter; The modeling framework for transmitters with non-negligible antenna array mutual coupling.

where $\boldsymbol{E}_k^{em}(\hat{\boldsymbol{r}})$ is the embedded element pattern of the antenna connected to the k-th PA, see Sec. 3.1.2. The other terms in this equation have been introduced in Sec. 3.1.

Finding incident signals to the antenna elements in an active antenna transmitter with coupled antenna elements is not trivial. In the k-th branch, $b_2^{(k)}$ depends on both the mismatch and the mutual coupling in the antenna array side as well as the PA input signal. Two incident waves into the PA, $a_1^{(k)}$ and $a_2^{(k)}$, define the output signal of the PA, $b_2^{(k)}$, which is also the incident wave to the k-antenna element. Analyzing the performance of active antenna transmitters requires correct implementation of the interactions between the antenna array and PAs. Fager [22, 66], Barradas [13], and Zakka [49] proposed techniques where the interaction between PA and antenna array are solved to find the value of the signal at the PA and antenna interface, i.e., $b_2^{(k)}$.

Fager, et al. [22, 66] developed a transmitter model which is formulated as $\mathbf{b} = f(\mathbf{a}, \mathbf{S}_{\text{ant}})$. This work suggests a closed-form analytical solution as the PA model is linear concerning the $\mathbf{a_2}$ waves. It is not straightforward to provide an analytical solution for the transmitter with more complicated PA models. Barradas et al. [13] implemented the PA and antenna S-parameter models in a MATLAB Simulink scheme such that the signal returning from an antenna array element, i.e., $a_2^{(k)}$, is fed back to the dual input PA model. A joint analysis scheme is thus provided to analyze the transmitter performance. In [49], the antenna active impedance is considered as PA output load. PA outputs, $b_2^{(k)}$, are determined using dual input PHD models.

The complexity and cost of digital beamforming architectures at mmWave frequency bands promote hybrid beamforming MIMO systems. Therefore, in Paper [A], we developed a hardware-oriented model for hybrid beamforming transmitters. In the following section, the proposed modeling technique is described. The proposed model

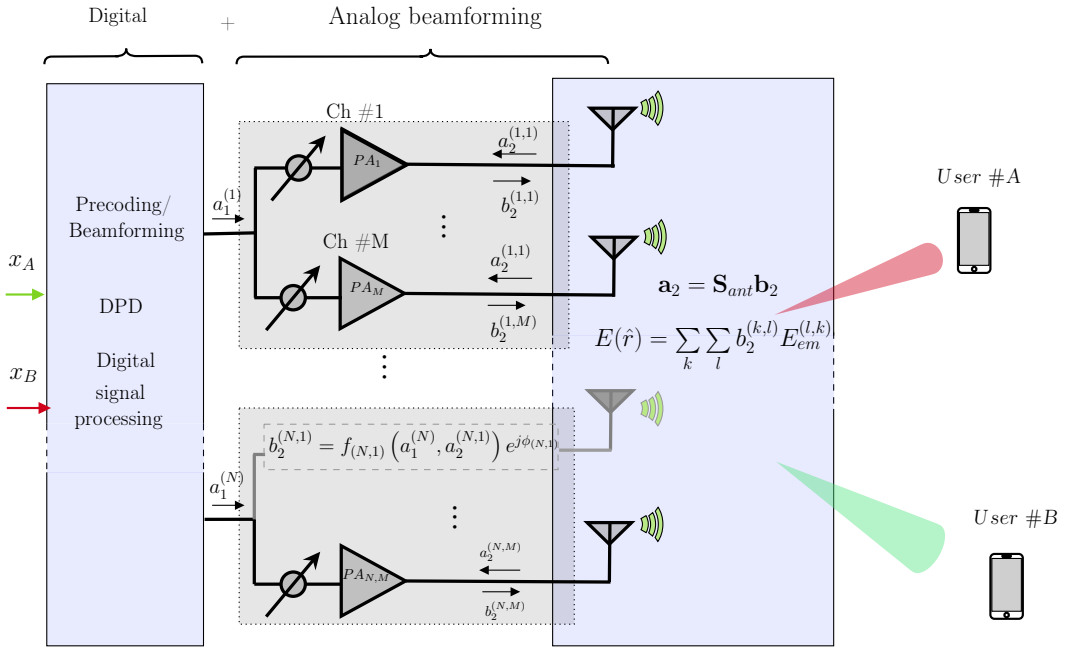

Figure 3.5: Hybrid beamforming MIMO transmitter; The architecture and modeling framework.

can be applied to both digital and hybrid beamforming architectures. However, the notation is developed for the hybrid beamforming transmitter case.

3.3.1 Model Algorithm

Fig. 3.5 shows the block diagram of a typical hybrid beamforming transmitter. In this configuration, beamforming is split into digital and analog beamforming domains. The hybrid beamforming transmitter has K RF transmit paths, each of them connected to an L-channel beamforming IC. Analog beamforming ICs perform amplification and phase shifting on the output channels. In total, there are LK RF output channels connected to the large-scale antenna array. Fig. 3.5 shows the analysis framework for the hybrid beamforming transmitter.

Here, instead of a PA, the model for the k-th channel of beamforming IC is described as

$$b_2^{(k,l)} = f_{(k,l)}(a_1^{(k)}, a_2^{(k,l)})e^{j\phi_{(k,l)}}, \quad \text{with} \quad l = 1:L, k = 1:K, \tag{3.12}$$

where the signal $a_1^{(k)}$ is the common input to the channels of the k-th beamforming IC. $a_2^{(k,l)}$ is the incident wave to the output of l-th channel of the k-th beamforming IC. $\phi_{(k,l)}$ is the analog beamforming phase shifts. $f_{(k,l)}(.)$ is the interpolation dual input model of l-th channel of k-th beamforming IC as introduced in Sec. 2.2.2. The antenna array model is similar to the one used in Sec. 3.3. Therefore, (3.10) represents antenna array mismatch and mutual coupling and (3.6) stands for antenna array radiated field.

In Paper [A] we propose an iterative algorithm to find $b_2^{(k,l)}$, see Algorithm 3.1. The iterative algorithm starts with the assumption of no reflection and no mismatch at the beamforming IC outputs, i.e. $a_2^{(k,l)} = 0$. In each iteration, (3.12) and (3.10) are evaluated. After a few iterations, N_{itr}, the algorithm converges to a steady value for $a_2^{(k,l)}$. Once $b_2^{(k,l)}$ are found, the total radiated field is calculated as

Algorithm 3.1 Iterative algorithm to obtain beamforming IC output

Input:

$a_1^{(k)}$	Input signals
$f_{(k,l)}$	Beamforming IC channels interpolation model
$\mathbf{S}_{\text{ant}}$	Antenna array S-parameters
$\phi_{(k,l)}$	Analog phase shifts
$a_{2,0}^{(k,l)} = 0$	Algorithm initialization ($i = 0$)

for i=0 to N_{itr} **do**
  for all k **do**
    for all l **do**
      $b_{2,i}^{(k,l)} = f_{(k,l)}(a_1^{(k)}, a_{2,i}^{(k,l)})e^{j\phi_{(k,l)}}$
    end for
  end for
  $\mathbf{b_2} = [b_{2,i}^{(1,1)}, ..., b_{2,i}^{(1,L)}, b_{2,i}^{(2,1)}, ..., b_{2,i}^{(K,L)}]^T$
  $\mathbf{a_2} = \mathbf{S}_{\text{ant}}\mathbf{b_2}$
  with
  $\mathbf{a_2} = [a_{2,i+1}^{(1,1)}, ..., a_{2,i+1}^{(1,L)}, a_{2,i+1}^{(2,1)}, ..., a_{2,i+1}^{(K,L)}]^T$
end for
Output:

$b_2^{(k,l)}$	Output signals for all n, $l = 1 : L$ and $k = 1 : K$.

$$\boldsymbol{E}(\hat{\boldsymbol{r}}) = \sum_{k=1}^{K}\sum_{l=1}^{L} b_2^{(k,l)} \boldsymbol{E}_{em}^{(k,l)}(\hat{\boldsymbol{r}}), \tag{3.13}$$

where $\boldsymbol{E}_{em}^{(k,l)}$ are embedded element patterns of the antenna elements introduced in Sec. 3.1.2 and used in (3.11) The algorithm runs per time step n to evaluate hybrid beamforming transmitter performance with modulated signal inputs.

Active Impedance

The changes in impedance seen by each PA (antenna active impedance) impacts the PA output and, therefore, the signal radiated by the antenna array. In Sec. 3.1.2 the active impedance is introduced assuming ideal array excitation. The actual active

reflection coefficient, considering the impacts of the antenna array and PA interactions, is calculated as

$$\Gamma_{\text{actual}}^{(k,l)} = \frac{a_2^{(k,l)}}{b_2^{(k,l)}(a_1^{(k)}, a_2^{(k,l)})}, \tag{3.14}$$

where $b_2^{(k,l)}$ are calculated using Algorithm 3.1. Paper [A] illustrates that the active reflection coefficient obtained from (3.14) of the evaluated hybrid beamforming subarray module differs significantly from the traditional case, where PA load dependence is ignored.

3.4 Active Antenna Transmitter Demonstrator

The accuracy of the proposed method explained in Sec. 3.3 was evaluated using measurements of a 29 GHz hybrid beamforming subarray module. First, the beamforming IC and the subarray antenna were characterized. Then the proposed iterative algorithm predicts the subarray module performance for various beam steering scenarios. In the next step, Over-The-Air (OTA) measurements were conducted to confirm the predicted results in terms of the radiation pattern and far-field nonlinear distortion. Paper [A] presents validation measurements for the beam steering scenario. However, the proposed modeling can be also applied to a hybrid digital and analog beamforming scenario if proper digital and analog weights are applied to the transmit signals.

3.4.1 Hardware Configuration

Fig. 3.6(a) shows the hardware configuration of a typical hybrid beamforming transmitter built by 2×2 subarray antennas, driven by individual beamforming ICs. A beamforming IC is a multi-channel device that includes Tx/Rx blocks integrated into an RF frontend. The TX/RX blocks include phase shifters, T/R switches, attenuators, PAs, and low noise amplifiers, see Fig. 3.6(b). Beamforming ICs typically apply independent analog beamforming weights to each of the output channels.

In Paper [A], the test case is a subarray module consisting of a 29 GHz 2×2 planar microstrip patch antenna array connected to a quad-channel beamforming IC from NXP Semiconductors. The beamforming IC operates at 26.5-29.5 GHz. Fig. 3.6(c) shows a picture of the tested subarray module. The beamforming IC was placed at the backside of the subarray antenna in the performed measurement.

3.4.2 Experimental Setup and Scenarios

As described in Sec. 2.2.4, the static model of the beamforming IC was identified using passive load-pull measurements performed at 29 GHz and with the help of the linear interpolation function of MATLAB. The measured antenna array S-parameters

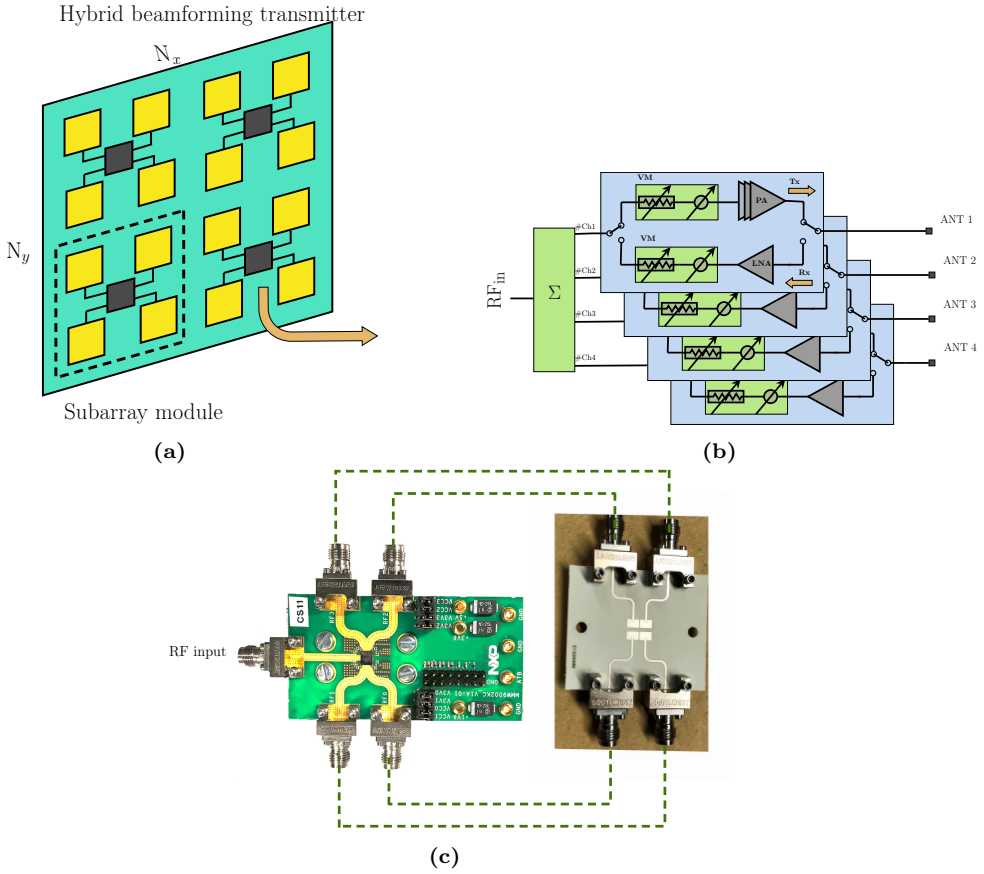

Figure 3.6: a) Hybrid beamforming transmitter and its building blocks, b) Block diagram of the beamforming IC, c) figure of implemented subarray module including evaluation board of the quad channel beamforming IC and 2×2 subarray antenna.

and EM simulated embedded element patterns were used in the modeling framework shown in Fig. 3.5. The maximum measured coupling happened between side-by-side elements and was around -12 dB. The antenna array and load-pull characterization procedure are described in detail in Paper [A]. OTA measurements were performed to validate the proposed transmitter modeling approach, see Fig. 3.7. The transmitter was the 2×2 subarray module, and a single antenna was the receiver. A VNA was used to generate a single tone signal at 29 GHz and to receive it.

In one measurement scenario, the distortion of the radiated signal was evaluated versus different steer angles. Fig. 3.7(a) shows the OTA block diagram for assessing far-field nonlinear distortion. The subarray module, as the transmitter, is set to steer the beam to $|Az_s| < 80°$, $|El_s| < 75°$. The input power was swept from -22 to 3 dBm to push the PAs of the beamforming IC a few dB into compression. The OTA measurements of AM/AM and AM/PM characterize the radiated signal distortion in the far-field.

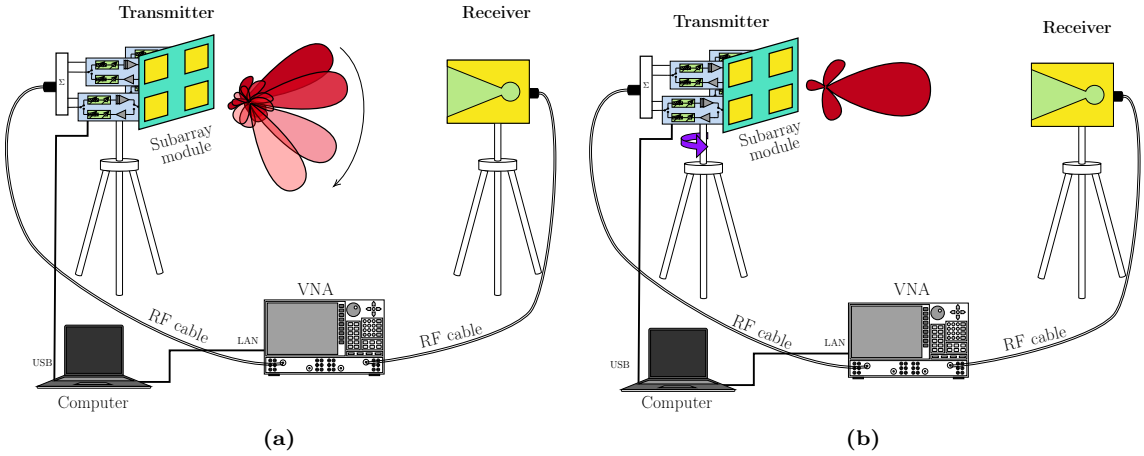

Figure 3.7: Block diagram of the setup for a) far-field signal distortion measurement, b) radiation pattern measurement.

The transmitter was set to steer the beam at three specific angles in another measurement scenario. The radiation pattern in the x-z plane was measured for the three specific angles. Fig. 3.7(b) illustrates the block diagram for radiation pattern measurement. Both measurement scenarios validate the effectiveness and accuracy of the proposed transmitter modeling.

3.4.3 Measurement results

In this section, the experimental results related to the scenarios introduced in Sec. 3.4.2 are presented. Results include radiation pattern and AM/AM and AM/PM distortions in the far-field.

Far-Field Signal Distortion

The OTA measured AM/AM and AM/PM distortion results correspond to the amplitude and phase of the received signal versus input power to the subarray module, see Fig. 3.7(a). The amplitude and phase variation of the calculated far-field radiation pattern represents the modeled AM/AM and AM/PM distortion. The difference between small signal and peak power gain and phase is denoted as *amplitude and phase compression* to quantify the AM/AM and AM/PM distortion behavior with two single values.

Fig. 3.8 shows the normalized received power, amplitude- and phase compression variation for different azimuth and elevation steering angles, $|Az_\mathrm{s}| < 80°$, $|El_\mathrm{s}| < 75°$. The measured results indicate that nonlinear distortion is dependent on steering angle. The RMS error as difference between simulation and measurement values of the amplitude and phase compression is about 0.18 dB and 1.6 degrees, respectively. Given the uncertainty in the measurement setup, the difference between the predicted

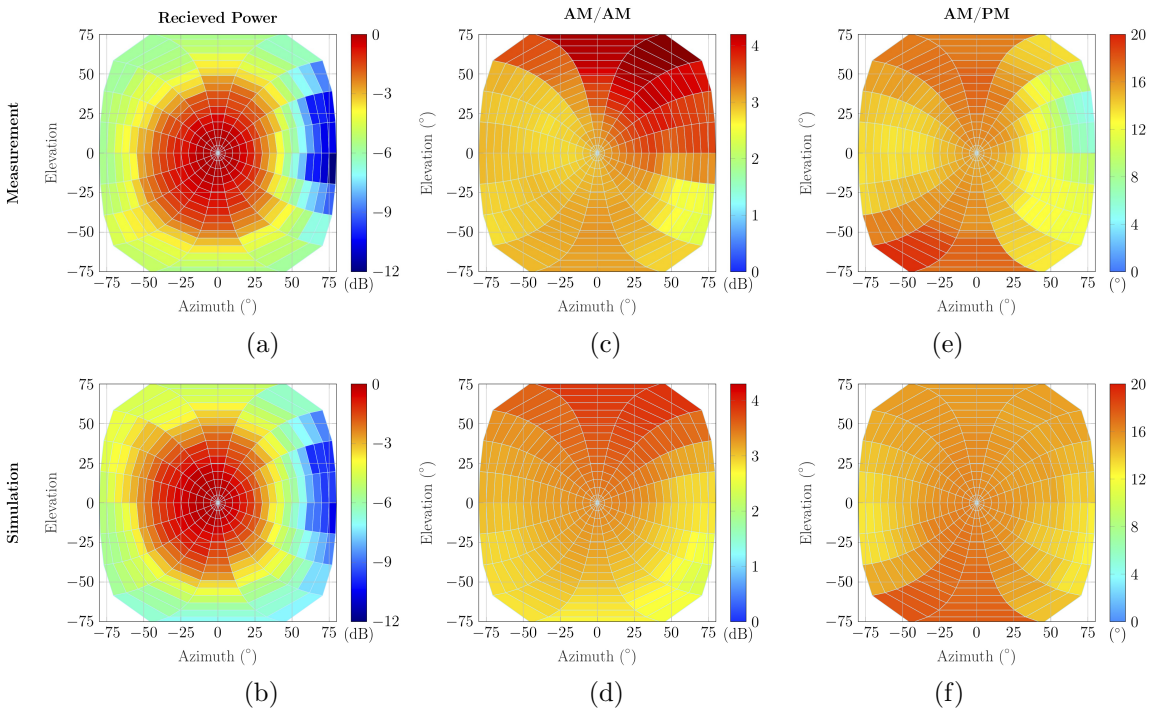

Figure 3.8: Normalized received power together with amplitude and phase compression variation in the far-field for different azimuth and elevation steering angles, $|Az_s| < 80°$, $|El_s| < 75°$. Normalized received power: a) OTA experiment b) Simulation. Amplitude compression: c) OTA experiment d) Simulation. Phase compression: e) OTA experiment f) Simulation. The RMS error between simulation and measurement of the amplitude and phase compression is 0.18 dB and 1.6 degrees, respectively.

and measured results is generally acceptable. Paper [A] presents more details about validation results.

Far-Field Radiation Pattern

Fig. 3.9 shows the measured and simulated radiation pattern for steered angles $El_s = 0°, Az_s = -30°, 0°, 30°$. The input power is 0 dBm to push the PAs into compression. Prediction results were obtained from (3.13) using simulation-based embedded element patterns. The PA nonlinearity and interactions with the antenna array have not affected the radiation pattern significantly. In [63], an unwanted sidelobe appears, which is probably due to a PA nonlinear effect on the antenna array performance. PA and antenna interactions strongly influence signal distortion, as is shown in Fig. 3.8. The presented method is effectively validated with a single tone CW measurement. The antenna array and beamforming IC must exhibit relatively constant characteristics within the signal bandwidth, as described in Sec. 2.1. If the signal bandwidth is relatively low, the method can also investigate the dynamic nonlinear behavior under modulated signal excitations.

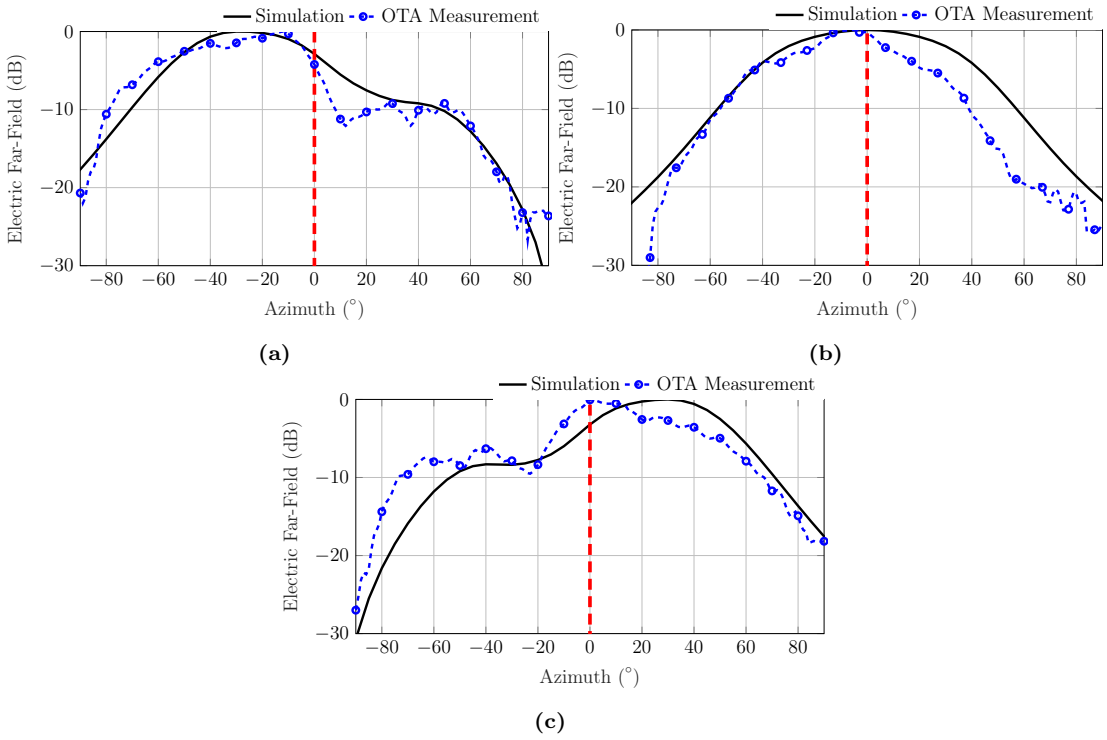

Figure 3.9: H-plane radiation pattern ($El = 0°$) versus steered angle: a) $(Az_s, El_s) = (-30°, 0°)$, b) $(Az_s, El_s) = (0°, 0°)$, The red dashed line shows the boresight angle.

3.5 Transmitter Linearity Prediction

Linearity is a critical requirement of any wireless transmitter. Most MIMO system transmitters use linearization algorithms, with a focus on DPD. There have been a variety of DPD techniques proposed for compensation of transmitter nonlinearity in MIMO systems [67–75]. A beam-dependent DPD approach has shown to be an efficient solution for hybrid beamforming transmitters [69, 71, 72]. Therefore, it is crucial to evaluate the transmitter performance along with DPD using a reliable transmitter model. Such investigations help develop DPD techniques and design suitable active antenna arrays for transmitters employing DPDs.

In this section, the linearity of large-scale hybrid beamforming transmitters with different configurations and sizes is assessed using the proposed algorithm in Sec. 3.3. An ideal beam-dependent predistorter is designed based on the predicted far-field static nonlinear distortion in a specific direction. The behavior of the linearized transmitter is evaluated for the beam steering scenario and in all steered beams. The transmitter model algorithm uses the antenna array S-parameters and embedded element patterns extracted from EM simulations. The beamforming IC is the one that was characterized in Sec. 2.2.4. In this study, the emphasis is not on developing a linearization or DPD technique. However, the potential of our proposed method is

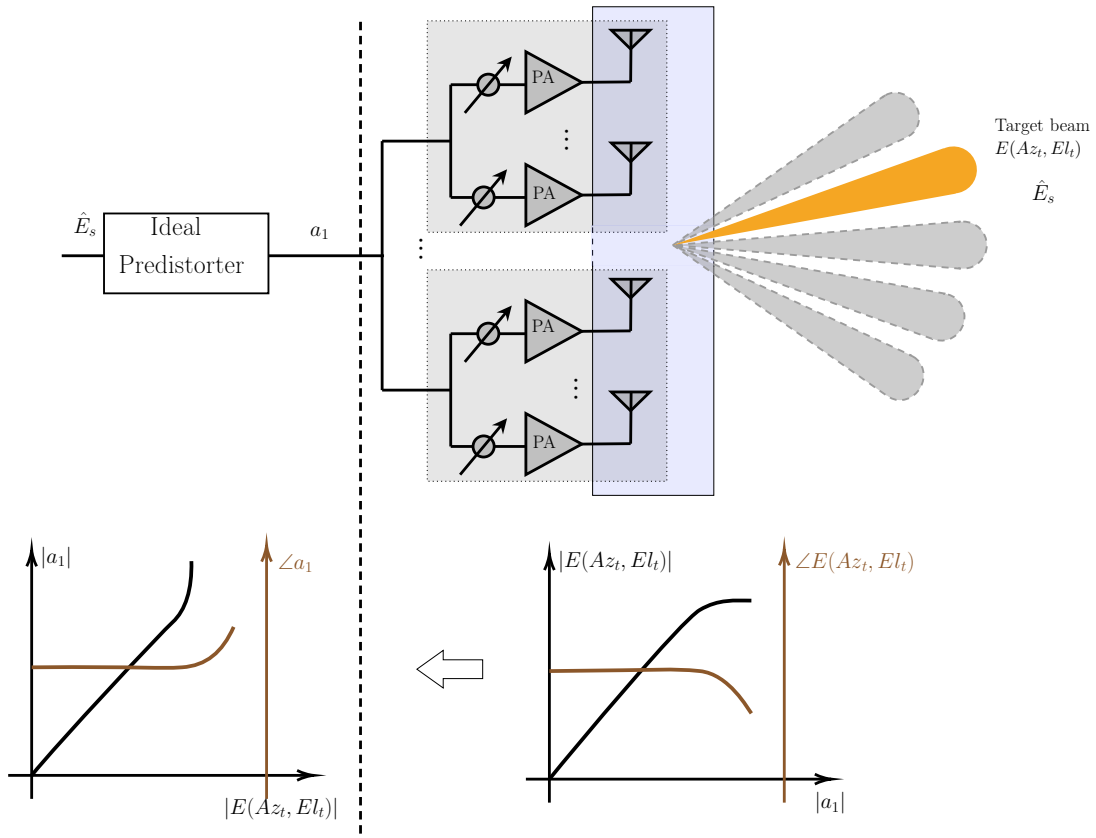

Figure 3.10: a) Structure of hybrid beamforming transmitter utilizing an ideal predistorter. b) The conceptual representation of the transmitter transfer AM/AM and AM/PM function and corresponding predistorter.

shown for the linearity analysis of large-scale hybrid beamforming transmitter systems where beam-dependent DPD is applied.

3.5.1 Analysis Method and Results

Fig. 3.10 illustrates the conceptual representation for developing the predistorter AM/AM and AM/PM functions. The considered ideal predistorter is designed to linearize the transmitter for one specific beam direction, i.e., (Az_t, El_t). First, the transmitter radiated far-field is evaluated for the target steered beam (Az_t, El_t). $E(Az_t, El_t, |a_1|)$ is obtained by applying the method described in Sec. 3.3. The power of the input signal is swept until the transmitter is a few dB in compression.

The function of the ideal predistorter is obtained by swapping input and output of the $E(Az_t, El_t, |a_1|)$ function. $|E(Az_t, El_t, |a_1|)|$ as the input, and $|a_1|$ as the output are interpolated to obtain the predistorter AM/AM function. The AM/PM predistorter function is the negative of $\angle E(Az_t, El_t, |a_1|)$.

Hybrid beamforming transmitters with two antenna array configurations $(N_x \times N_y)$,

8×8 and 16×4, are designed in CST and studied here, see Fig. 3.2 for the antenna configuration. The coupling level is -12 dB and -20 dB between elements in the x and y direction. Individual beamforming ICs drive each 2×2 subarray antenna. The beamforming IC is the one characterized in Sec. 2.2.4.

The behavior of the beamforming transmitter combined with the ideal predistorter is evaluated for all beam steering cases. $\hat{E}_s(n)$ is the desired far-field signal at the time instance n. $E_s(n)$ is the far-field signal at the main beam of each individual steered beam. A single carrier LTE communication signal with an 8.5 dB Peak-to-Average Power Ratio (PAPR) and 20 MHz bandwidth is selected as $\hat{E}_s(n)$. The normalized mean square error (NMSE) is considered as the figure of merit for evaluating the linearity of each steering beam. The NMSE is calculated by:

$$\text{NMSE} = \frac{\sum_{n=1}^{N} |\alpha E_{\text{s}}(n) - \hat{E}_{\text{s}}(n)|^2}{\sum_{n=1}^{N} |\alpha E_{\text{s}}(n)|^2}, \tag{3.15}$$

where N is the total number of time samples. α is a complex scaling factor which is calculated for each steered beam to eliminate the effects of gain and output power variations in different steering directions. The 16×4 transmitter is linearized for the steer angles $(Az_t, El_t) = (0, 0)^\circ, (50, 0)^\circ, (30, 25)^\circ$, and the 8×8 transmitter is linearized for $(Az_t, El_t) = (0, 0)^\circ$. Fig. 3.11 shows the linearity (NMSE) of the linearized transmitters for steered beam $|Az_s| < 80^\circ, |El_s| < 75^\circ$. In each configuration, in the direction (Az_t, El_t) the transmitter with ideal predistorter is ideally linear. It can be seen that the array configuration and coupling level between elements in x or y direction affects the linearity variation.

In this study, the nonlinear distortion is very low for all cases and steered beams. However, the NMSE variation between different beams is significant. The other observation is that linearity has a diagonal symmetry behavior because beams at (Az_s, El_s) and $(-Az_s, -El_s)$ are identical for an equally spaced ideal rectangular array. Generally, the linearity behavior relies on the specific beam direction, which is aimed to be fully linearized [69, 71, 72]. This is an important observation that should be carefully considered for a transmitter in the design stage.

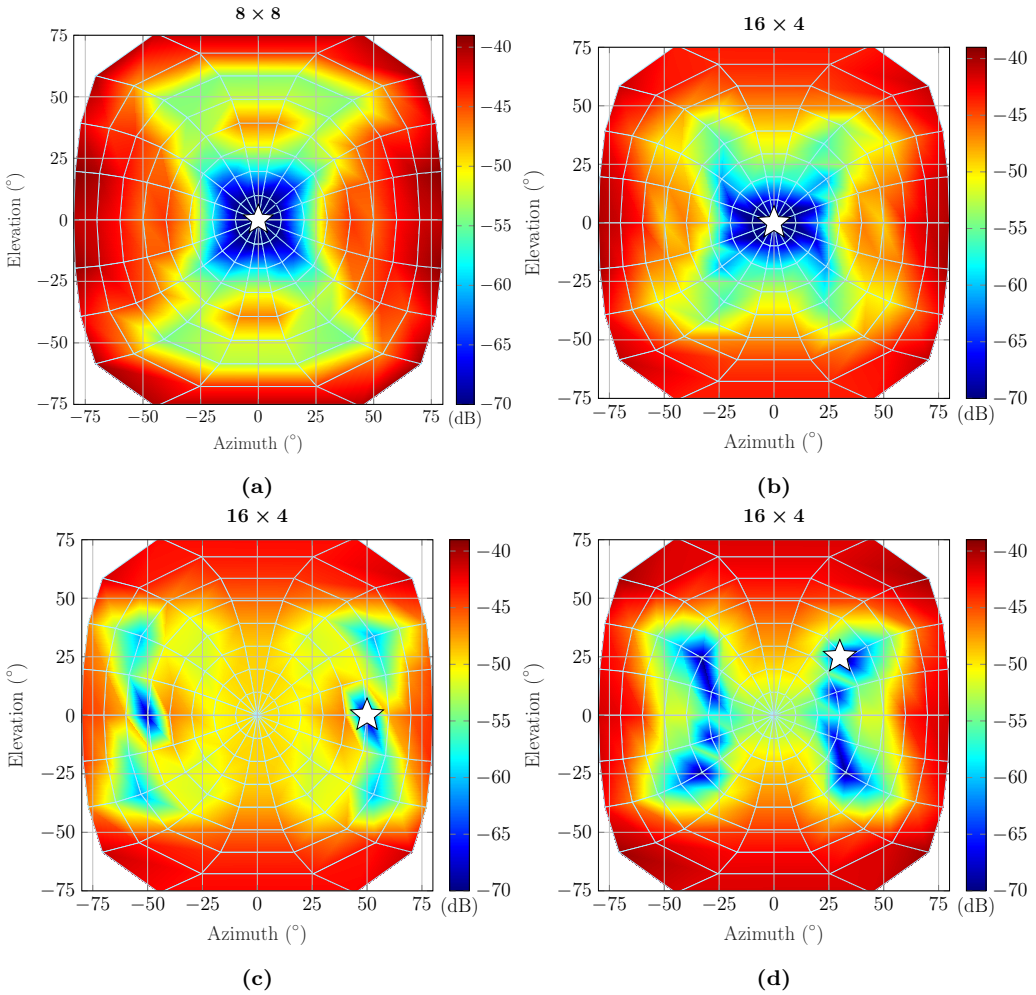

Figure 3.11: Nonlinear distortion in the far-field versus steering angle for a) 8×8 array linearized for the beam at $(Az_t, El_t) = (0, 0)°$, b) 16×4 array linearized for $(Az_t, El_t) = (0, 0)°$, c) 16×4 array linearized for $(Az_t, El_t) = (50, 0)°$, and d) 16×4 array linearized for $(Az_t, El_t) = (30, 25)°$. The results are presented in terms of normalized mean square error for an LTE signal with 8.5 peak-to-average power ratio. The white filled star represents the direction that the beam-dependent DPD is optimized for.

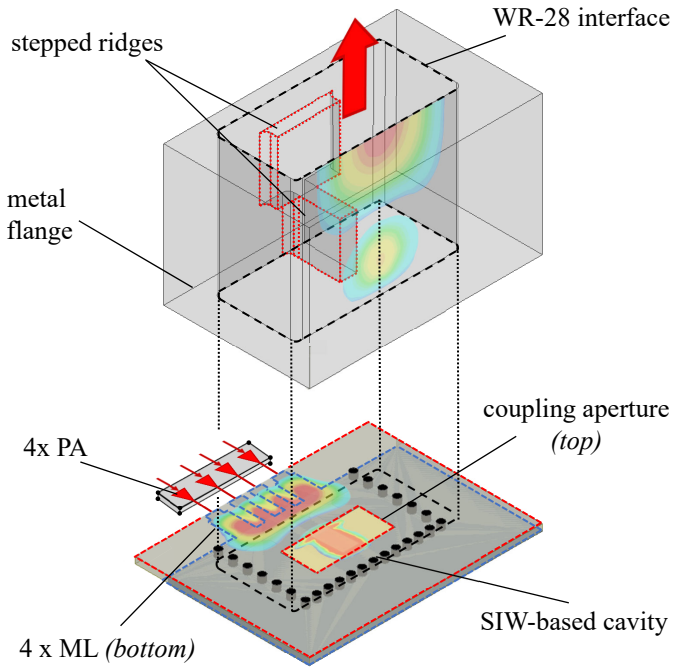

Figure 3.12: The configuration of the proposed spatial power-combining module in Paper [B].

3.6 Performance of an Active Power Combining Module

The higher path loss at mmWave frequencies can be compensated either by using a large number of PA and antennas or increasing power per branch or antenna element in active antenna transmitters. Typically, output power per antenna can be increased by combining the power of multiple active devices. A variety of on-chip power combining methods exist [76–80]. However, on-chip power combining networks suffer from high insertion losses, and the losses increase as the number of interconnected components increases. Paper [B], in continuation of [81], has proposed a novel power combining solution where an array of multiple power amplifiers are interfaced to a single Substrate Integrated Waveguide (SIW). The proposed combiner has low insertion loss, 0.4 dB. In this section, the active performance of the proposed power combining module is investigated. The interaction between the PA and combiner and the critical effects of coupled PAs is studied and experimentally evaluated using the combiner module with the introduced beamforming IC in Sec.3.4.1.

3.6.1 Spatial Power Combining Module

Fig. 3.6 shows the model of the power combining module structure. It employs an array of four microstrip lines exciting a SIW-based cavity. A conventional rectangular

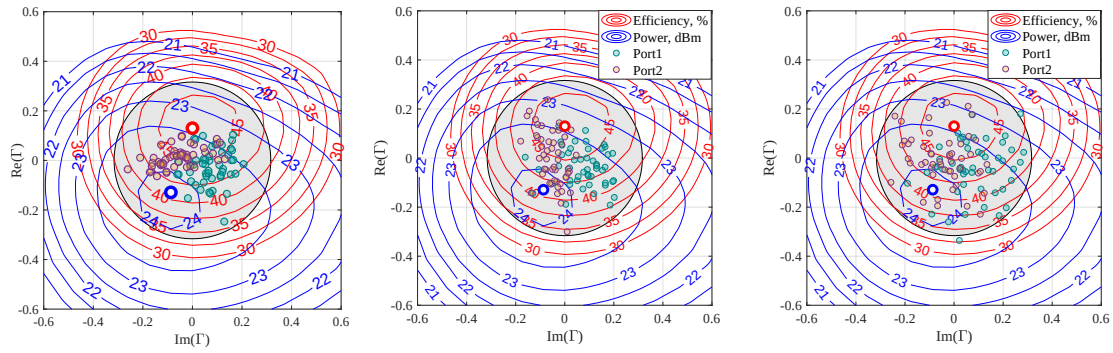

Figure 3.13: Efficiency (red) and P1dB output power (blue) contours of the simulated PA at 28 GHz in the load reflection coefficient plane. The cluster of points shows Γ_1 and Γ_2 of the power-combining module in the presence of (a) $\pm 15^o$ phase errors; (b) 1dB amplitude errors; (c) Both amplitude and phase errors with normal distribution.

waveguide interface is the output port of the combiner module to demonstrate the power combining and the interface to the waveguide port antennas. The electric field from the SIW-based cavity is coupled through the etched rectangular aperture into the WR-28 waveguide interface using a stepped ridge waveguide. More details about the design parameters are provided in Paper [B].

3.6.2 Joint PA and Combiner Performance Evaluation

PA characteristics such as output power, gain, and efficiency, are highly dependent on the PA output load. Load pull contours, as introduced in Sec. 2.2.4, predict the PA performance versus different loading conditions. When the PAs are coupled through non-isolated input channels of the power combiner module, the load represented to the output of each PA corresponds to the active reflection coefficient at the combiner input channel, i.e., Γ_i^{act}, see (3.7). Here, $S_{n,m}$ is the element of the combiner S-parameter matrix, and b_n is the complex gain of n-th PA.

In an ideal power combining condition, the PAs are assumed to behave similarly, and thus the combiner input channels have uniform amplitude and phase excitation; $b_n = b_m|_{n,m}$. This assumption was also the basis for designing the passive combiner in [81] without considering the PA and combiner interactions. However, PAs are non-identical in practice and show different gain and output phases due to fabrication errors and varying temperatures. Therefore, the active impedance of the combiner input channels deviates from its optimal value and thus, degrades each PA performance.

In Paper [B], the active performance of the power combining module in conjunction with the realistic PAs is investigated by both simulation and experiments. In a simulation scenario, the designed power combining module has been interfaced with four conventional single-ended common-base PAs, which have been designed in SiGe

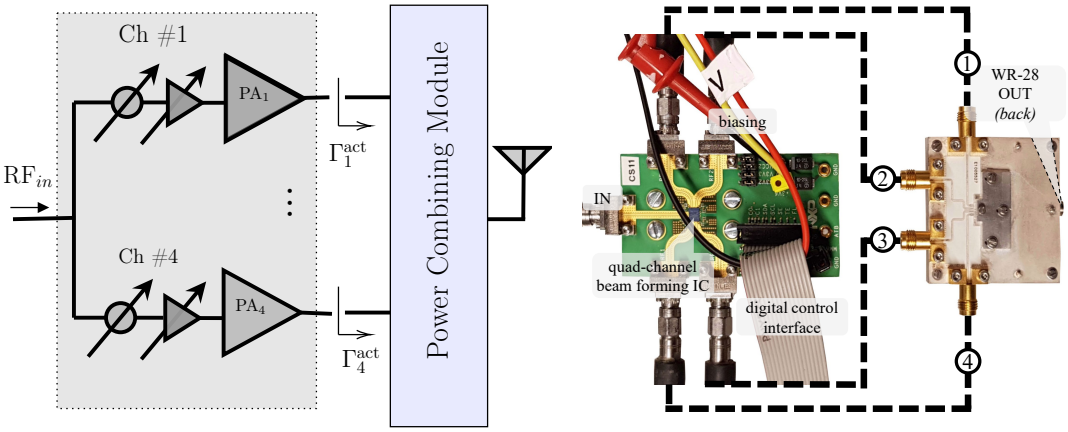

Figure 3.14: (a) Block diagram and (b) measurement setup for evaluating active performance of the power-combining module in conjunction with the beamforming IC; (vector network analyzer and cables are not shown).

BiCMOS technology. The experiment was performed using the manufactured power combining module in conjunction with the quad-channel beamforming IC with similar technology. The TX branches of the beamforming include a PA, a phase shifter, and a variable gain amplifier (VGA). The gain and phase of each branch can be changed via a digital control interface. The block diagram of the beamforming IC is provided in Sec. 3.4.1.

Fig. 3.13 shows the simulated load-pull contours of the designed PA in terms of output power in 1-dB compression point and efficiency, at 28 GHz frequency. The effect of non-identical PAs is emulated by applying normally distributed errors to the amplitude and phase of the combiner's input channels. The active impedance of channel-1 and 2 of the combiner are calculated using (3.7) and overlaid with the PA load-pull contours. Fig. 3.13 shows that the active impedance variations remain in the region of high output power and high efficiency of the designed PA. This study shows the combiner sensitivity to the non-uniform excitation and can determine design guides for maximum allowable PA output phase and amplitude variation. The results show that for amplitude and phase variations within $\pm$1dB and $\pm 15^o$ ranges, respectively, the output power reduces less than 1 dB.

The quad-channel beamforming IC has been interfaced with the fabricated power-combining module to experimentally evaluate combining performance in the presence of non-identical realistic PAs. Fig. 3.14 shows the measurement block diagram in which four short coaxial cables connect the evaluation board of the beamforming IC to the combiner. The gain and phase of each channel can be controlled via a digital control interface. This ability has been used to drive the power combining module with equal amplitude and phases distribution and present errors corresponding to emulating non-identical PAs. Fig. 3.15 shows the measured coupling between input

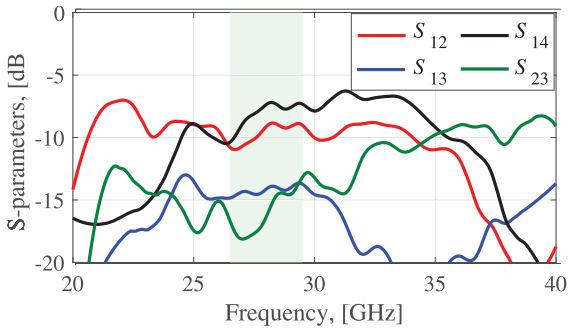

Figure 3.15: Measured mutual coupling level between the input ports of the power combining module. The colored region shows the operation band of the PAs.

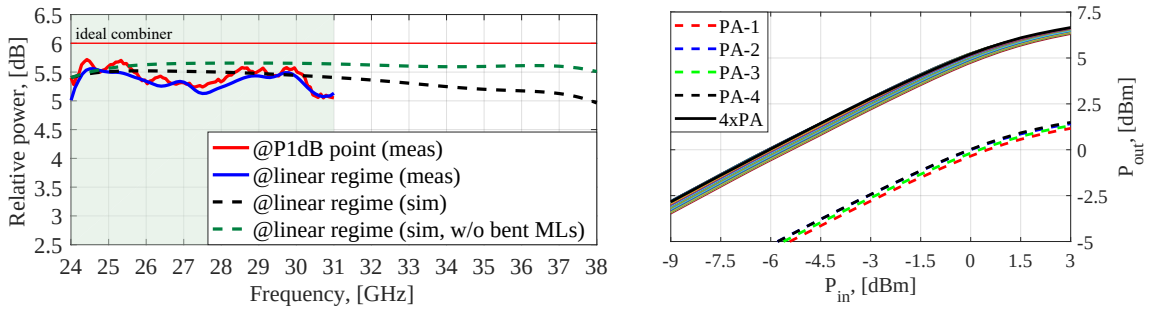

(a) **(b)**

Figure 3.16: (a) Simulated (dashed) and measured (solid) relative increase of the generated output power of the 4×PA combined by the proposed module, at P1dB and in the linear region. (b) Measured output power versus input power for single PAs (dashed) and after combination with the combiner module (solid) at 28 GHz. Both input and output powers are normalized to obtain 0 dB gain at P1dB point for a single PA. The set of curves shows measured combining degradation in the presence of $\pm 15^o$ phase variation.

channels of the combiner. The non-negligible coupling among input channels affects the active input impedance in the presence of non-uniform excitation.

Fig. 3.16(a) shows the measured and simulated increase of the combined output power of the 4× PA concerning a single PA. The results present the relative power increase in PAs' linear and nonlinear working regimes at 24-31 GHz frequency bandwidth. The simulated results are obtained from EM simulation, including dielectric losses. Overall, the measured results are close to simulation. The lower combiner gain is due to the losses in the extended routing of the microstrip lines.

Fig. 3.16(b) presents the measured combined power in comparison with the single PA performance. As it can be seen, the joint PAs and combiner nonlinear behavior is similar to that of a single PA. Phase shifts of each beamformer channel have been manually adjusted to assess combining performance degradation in the presence of phase errors. The set of semitransparent curves shows the measurement results related to $\pm 15^o$ of phase variation. The output combined power decrease by less than 1

dB in the worst-case scenario. These results are in agreement with simulation, see Fig. 3.13. The combining performance of the proposed spatial power combing module is found in acceptable limit with $\pm 15^o$ and 1 $\pm 1dB$ phase and gain error considering the interaction between combiner and PAs. Such investigations play an essential role in the design and accurate analysis of high-power mmWave transmitters.

3.7 Summary

In this chapter, an introduction to antenna array theory and the coupling effects in antenna array characteristics are first described. A modeling technique is then proposed, and its iterative algorithm for the analysis of active antenna transmitters is explained. The experimental validation scenarios and obtained results are presented. Furthermore, the proposed transmitter analysis method is applied to predict the linearity of large-scale transmitters when an ideal beam-dependent linearization is used. Finally, the active performance of a spatial power combining module is predicted and experimentally validated, considering the interaction between PAs and the combiner module. The joint PA and combiner analysis help define design guides for PA allowable error range in output phase and amplitude and coupling between combiner's channels. In this chapter, circuit performance of PA and EM characteristics of antenna array/power combiner were jointly considered in the active antenna transmitter analysis framework. However, another crucial factor impacting transmitter performance is heat dissipation and temperature variations. Thermal issues mainly originate from PAs in transmitters. In the next chapter, thermal issues in the transmitter are addressed, and efficient methodologies for modeling the electrothermal behavior of PAs are presented.

Chapter 4

Electrothermal Modeling of Power Amplifiers

PAs dominate the heat dissipation and thermal issues in active antenna transmitters. Apart from reliability and thermal management challenges, PA performance is highly temperature-dependent. Therefore, to accurately predict the performance of an active antenna transmitter, it is required to obtain the static and dynamic electrothermal performance of PAs. Joint circuit-thermal simulation of PAs using CAD tools is a time-consuming and computationally complex procedure. Instead, methodologies based on behavioral models that can avoid either one or both of complicated and detailed simulations are favorable.

This chapter introduces methods for the electrothermal analysis of complex PA ICs following the thermal modeling approach. First, an overview of the importance of thermal modeling is given. The concept of the thermal impedance matrix and a corresponding identification algorithm is described. Next, two methods for electrothermal analysis using the extracted thermal model are proposed and explained. The circuit-based electrothermal analysis uses an equivalent thermal network and combines it into electrical solvers such as Keysight ADS or Spice. The temperature-dependent PA behavioral model introduced in Sec. 2.2.3 is combined with a thermal impedance matrix to perform behavioral model-based electrothermal analysis in a second approach. The proposed methodologies have been verified using the experimental evaluation of a PA DUT's static and dynamic performance. The chapter ends with a summary.

4.1 Importance of Thermal Modeling

The thermal issue is one of the critical factors limiting the performance and reliability of PA ICs and active antenna transmitters. Due to the high level of integration, and therefore power density growth, thermal issues increasingly degrade the steady-state and dynamic operation of PA ICs [20, 82, 83]. Therefore, a reliable electrothermal

analysis that simultaneously solves the coupled electrical and thermal problems is greatly needed to accurately predict the PAs and, consequently, the transmitters' performance under realistic conditions.

Commonly employed approaches for electrothermal analysis rely on interactions between a circuit simulator and a numerical thermal-only CAD tool in a relaxation cycle [84–89]. A thermal solver calculates the device temperature using FEM or finite difference (FD) techniques by solving heat equations. Simultaneously, an electrical solver analyzes the circuit and calculates the device dissipated power. Temperatures and dissipated powers are exchanged between the two solvers until a self-consistent solution is found in each electrical simulation point. Such coupled approaches depend on the convergence of the iterative loop between both solvers. Accordingly, the use of coupled electrical- and individual thermal solvers to evaluate the performance of complex electronic circuits becomes extremely time-consuming and computationally cumbersome.

Different modeling techniques have been developed to avoid the computational complexity of FEM thermal simulations in an electrothermal analysis. A thermal model is an analytical representation which can be represented by an equivalent thermal network best compatible with circuit simulators. It is well known that an equivalent thermal network can directly describe discretized heat diffusion problems [20, 90, 91]. However, a direct transformation may result in a large equivalent thermal network. Therefore, a variety of Model Order Reduction (MOR) techniques have been proposed to reduce the size of the equivalent thermal network [92–99]. Although the thermal network size can be reduced considerably by employing MOR techniques, the computational complexity for electrothermal simulation of complex electronic circuits remains high.

Compact thermal model (CTM) identifications is a way to develop less complex thermal equivalent networks [19, 20, 91, 100–103]. A CTM describes the thermal behavior of the device at the desired regions using the concept of a thermal impedance matrix. Such approaches provide flexibility in which a trade-off between model complexity and accuracy can be obtained [19, 20]. A thermal network or an analytical thermal model can be identified using the step response of a thermal system at the prescribed input/output ports.

4.2 Thermal Model Identification

The heat propagation in a medium occurs in three different ways: conduction, convection, and radiation. In an electronic circuit, the heat propagation mechanism is dominated by conduction. A parabolic partial differential equation defines the general heat conduction equation in a homogeneous isotropic medium as [91]:

$$c(\mathbf{r})\frac{\partial T}{\partial t}(\mathbf{r},t) - \nabla \cdot (k(\mathbf{r})\nabla T(\mathbf{r},t)) = F(\mathbf{r},t) \tag{4.1}$$

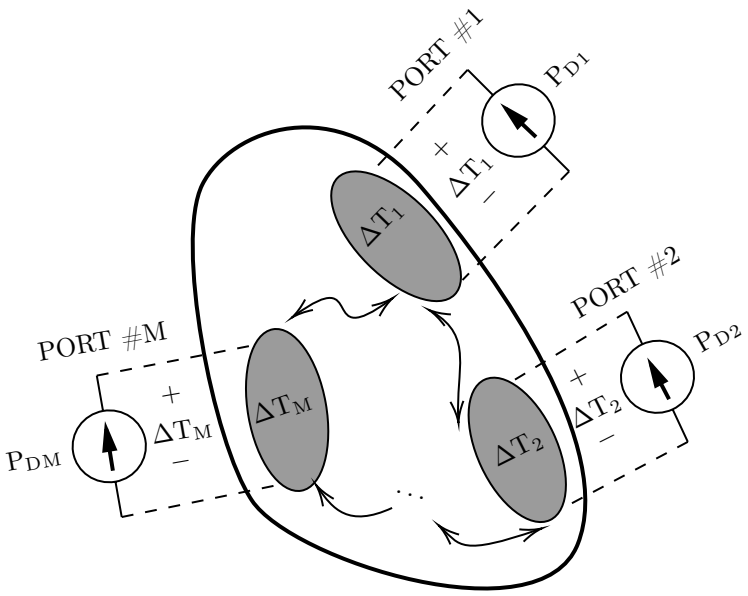

Figure 4.1: Representation of the compact thermal model for a thermal problem with designated heat sources.

where ∇ is the gradient with respect to the spatial coordinates, $\mathbf{r}$. $T(\mathbf{r}, t)$ is the temperature rise with respect to the ambient temperature and $F(\mathbf{r}, t)$ is the power distribution. $k(\mathbf{r})$ is the material thermal conductivity and $c(\mathbf{r})$ is the volumetric heat capacity.

It is well established that a reciprocal and passive thermal network model can represent the discretized heat equation. Here, following the CTM approach, the thermal impedance matrix and the proposed identification algorithm in Paper [C] are introduced.

Fig. 4.1 shows a device with M designated areas as heat sources. The thermal behavior of the device, assuming a linear thermal problem, is described by the $M \times M$ thermal impedance matrix $\mathbf{Z}_{th}(t)$. The elements of the thermal impedance matrix, $z_{th,ij}(t)$, are defined as normalized step responses, i.e. temperature rise $\Delta T_i(t)$ of the i^{th} heat source due to applying a power step to the j^{th} heat source, P_j.

$$z_{th,ij}(t) = \frac{\Delta T_i(t)}{P_j}, \tag{4.2}$$

$$\Delta T_i(t) = T_i(t) - T_{\text{amb}}$$

where T_{amb} is the ambient temperature. $z_{th,ii}$ is the self-heating thermal impedance, and $z_{th,ij}$, $i \neq j$ is indicating thermal coupling between heat sources.

The thermal impedance matrix can be modeled with both time- and frequency domain functions. Specifically, it has been shown that an equivalent Foster network can be used to synthesize the transfer function of a standard thermal problem [104].

Algorithm 4.1 The thermal modeling identification algorithm

Input:

$\widetilde{\mathbf{Z}}_{th}$	The thermal step response data
$\mathbf{Z}_{th}(t, \tau_n, c_{n,ij})$	Model of the thermal impedance matrix
$\tau_n^{(0)}, n = 1, ..., N_m$	Initial guess for time constants
$\mathbf{Z}_{th}(t, \tau_n^{(0)})$	Initialized value of the thermal impedance

while $||\mathbf{Z}_{th}(t, \tau_n^{(k)}, c_{n,ij}^{(k)}) - \widetilde{\mathbf{Z}}_{th}|| < \epsilon$ **do return** False

$c_{n,ij}^{(k)} = \text{argmin}||\mathbf{Z}_{th}(t, \tau_n^{(k-1)}) - \widetilde{\mathbf{Z}}_{th}||$[1] using NNLS[2]

with $c_{n,ij}^{(k)} \geq 0$

$\tau_n^{(k)} = \text{argmin}||\mathbf{Z}_{th}(t, c_{n,ij}^{(k)}) - \widetilde{\mathbf{Z}}_{th}||$ using NLLS[3]

$k = k + 1,$

end while

Output:

$\mathbf{Z}_{th}(t, \tau, c_{n,ij})$	Identified thermal impedance model

Therefore, by considering a finite-sized Foster network, the elements of the multi-port thermal impedance are written in the time domain as

$$z_{th,ij}(t) = \sum_{n=1}^{N_m} c_{n,ij}(1 - e^{-\frac{t}{\tau_n}}) \tag{4.3}$$

where N_m is the number of time constants τ_n. $c_{n,ij} \geq 0$ and $\tau_n > 0$ are to guarantee passivity of the obtained solution [20, 104]. It is assumed that the thermal system is linear and time-invariant. The time constants, i.e., τ_n, are common throughout the structure while the model linear coefficients, $c_{n,ij}$, are unique for each element of the thermal impedance matrix.

Algorithm 4.1 describes the proposed iterative algorithm in Paper [C] for identifying the time constants and coefficients of the thermal impedance model as are introduced in (4.3). $\widetilde{\mathbf{Z}}_{th}$ is the $M \times M$ matrix of observed step responses of the thermal system generated from 3-D FEM thermal simulations. The model linear- and nonlinear coefficients, $c_{n,ij}$ and τ_n, are found using nonlinear- and non-negative least square, respectively. A regular pseudo-inverse solution cannot find linear coefficients due to non-negativity limitations. The algorithm stops if the residue or fitting error has stabilized to a minimum value, i.e., $||\mathbf{Z}_{th}(t, \tau_n^{(k)}, c_{n,ij}^{(k)}) - \widetilde{\mathbf{Z}}_{th}|| < \epsilon$.

[1] $||.||$ is the 2-norm matrix operator

[2] Non-negative least square method.

[3] Nonlinear least square method

4.3 Equivalent Thermal Network

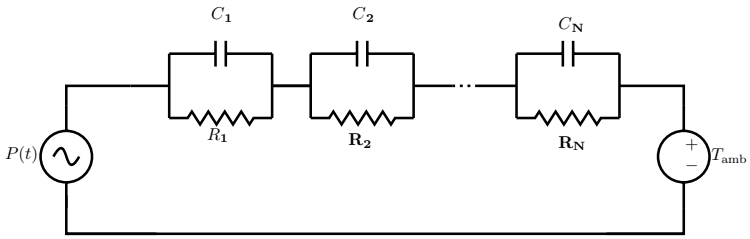

Figure 4.2: Foster RC equivalent circuit for self heating.

Electrical solvers such as ADS and Spice require an equivalent thermal circuit to perform coupled electrothermal analysis. Therefore, it is crucial to provide an equivalent circuit topology that is also compatible with standard circuit simulators. Fig. 4.2 shows the Foster RC equivalent circuit for representing self-heating impedance in a single port thermal problem, i.e. $M = 1$ and $z_{th,11} = z_{th}$. The value of resistors and capacitors, according to the thermal model in (4.3), are obtained as:

$$\begin{aligned} R_n &= c_n \\ C_n &= \frac{\tau_n}{c_{n,11}} \end{aligned} \tag{4.4}$$

The synthesis of a multi-port impedance matrix is not directly feasible, having time- or frequency domain representation of $\mathbf{Z}_{th}$. Proper circuit topology and elements are required to model the thermal coupling between ports. In [20, 91] the thermal impedance matrix is synthesized by means of N_m capacitors, N_m resistors and $N_m \times M$ ideal transformers. In [21] a circuit topology including Voltage Control Current Source (VCCS), resistors, and capacitors to synthesize multi-port thermal impedance is proposed. Paper [C] used VCCSs, Current Control Current Sources (CCCS), and resistors for thermal network synthesis. It is described that the elements of the thermal impedance matrix, $z_{th,ij}$, represent the thermal system step response. For the thermal network extraction, the frequency domain representation of the system impulse response, $z_{imp,ij}$, is more suitable and is given by

$$z_{imp,ij}(s) = \sum_{n=1}^{N_m} \frac{c_{n,ij}}{1 + \tau_n s} \tag{4.5}$$

The proposed thermal equivalent circuit in Paper [C] connects each thermal node to 1 (K/W) resistors in parallel with M VCCSs. The VCCS values are equal to $z_{imp,ij}$ for $j = 1, ..., M$ if $i \neq j$, and $z_{imp,ii} - 1$ for $i = j$. The corresponding controlled voltages of VCCSs are created using an extra node connected to a CCCS with the value of 1 in parallel with a 1 (K/W) resistor. The related controlled current is equal

to P_i. The VCCS in the proposed equivalent circuit is compatible with HSpice Foster pole-residue format [105] and can be conveniently presented in the frequency domain using (4.5). The thermal networks have $2 \times M$ nodes, which will be added to the electric circuit netlist. The number of nodes is proportional to the number of heat sources. Therefore, increasing model order, i.e., number of time constants, does not increase the complexity of the thermal network. However, the number of nodes using the RC Foster network is directly proportional to the model order and the number of heat sources [20, 91]. Therefore, our proposed topology is highly efficient for adding into the circuit simulator for electrothermal analysis.

4.4 Methods for Electrothermal Analysis

As it is explained in Sec. 4.1, the use of coupled electrothermal simulation, particularly by using dedicated CAD tools, is time-consuming and computationally complex. The computational complexity and speed of electrothermal simulations can be significantly improved by using thermal models or equivalent thermal networks rather than running 3-D FEM thermal CAD tools.

In Paper [C], two efficient electrothermal analysis approaches are presented based on the thermal modeling of PAs. The circuit-based electrothermal analysis refers to a circuit simulation that includes an equivalent thermal network and can provide temperature-aware simulation results. On the other hand, the behavioral model-based approach utilizes the introduced temperature-dependent PA behavioral models in Sec. 2.2.3 and combines them with the thermal impedance matrix in an iterative algorithm.

4.4.1 Circuit-based Electrothermal Analysis

Fig. 4.3(a) shows the steps for performing the circuit-based electrothermal simulation. Areas related to the temperature-dependent circuit elements, such as transistors and resistors, are chosen as heat sources. The thermal netlist can be created following the thermal modeling approach and equivalent thermal network extraction that are presented in Sections 4.2 and 4.4, respectively. Finally, the netlist of the thermal equivalent network can be integrated as a sub-circuit into the PA electrical circuit netlist. Fig. 4.3 (b) presents the interaction between thermal network and electrical circuit inside an electrothermal netlist. As it can be seen, the temperature-dependent circuit elements are equipped with an additional node for temperature as input and dissipated power as the output. In this way, power and temperature are exchanged between the thermal network and the electrical circuit. Therefore, the elements with temperature-dependent nodes are updated with correct temperature values while the effect of self-and mutual heating is accurately accounted. Ultimately, the temperature-aware performance of the PA circuit is obtained using the proposed circuit-based

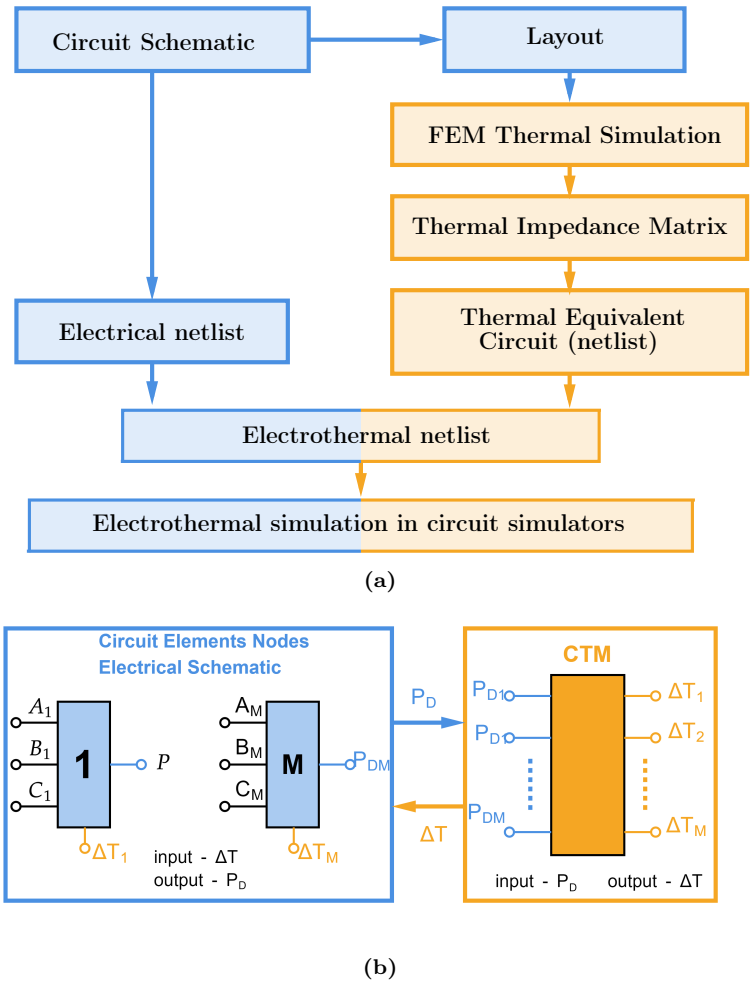

Figure 4.3: Electrothermal analysis using equivalent thermal network. a) Analysis-flow, b) Electrothermal netlist; conceptual representation of temperature and power exchanges, A,B,C shows electrical nodes of the temperature-dependent elements [21].

electrothermal analysis method.

4.4.2 Model-based Electrothermal Analysis

The circuit-based electrothermal analysis presented in Sec. 4.4.1 is relatively faster than the coupled CAD simulations since the iteration loop between two solvers is removed. However, the circuit-based electrothermal simulation still takes too long for circuit simulations with modulated signal excitations. An alternative approach is to use PA temperature-dependent nonlinear behavioral model for electrothermal analysis combined with its thermal model. In [26, 27, 52] a system-level circuit/EM/thermal analysis method is proposed in which the PAs self-heating models are coupled with nonlinear behavioral models in a multi-branch transmitter. In Paper [C], we have adopted the proposed approach for electrothermal analysis of a single PA having a

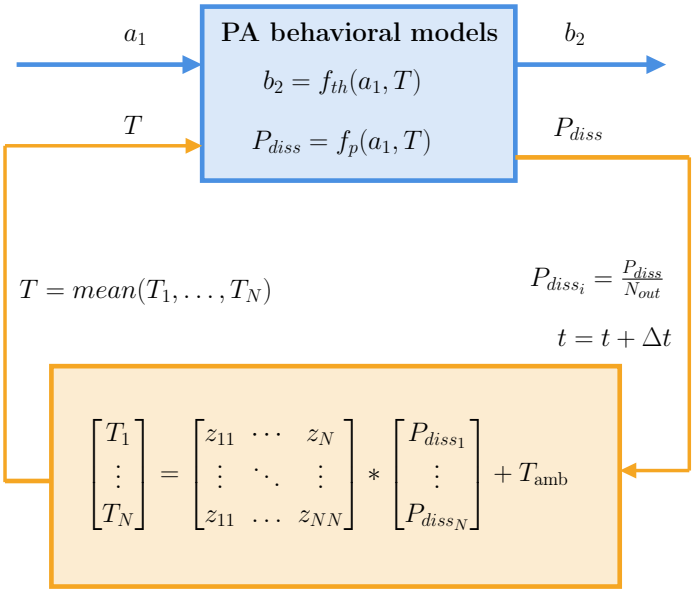

Figure 4.4: The behavioral model-based electrothermal analysis approach. N_{out} is the number of PA output transistors and $*$ is the convolution symbol. For simplicity the time dependency of b_2, a_1, P_{diss}, temperature and thermal impedance matrix is not shown.

multi-port thermal impedance model.

The joint simulation algorithm for the behavioral model-based electrothermal analysis is illustrated in Fig. 4.4. It is important to note that the behavioral model-based electrothermal analysis operates in the complex envelope/modulation time domain and therefore describes the behavior around a given center operating frequency. This method is developed based on combining temperature-dependent PA behavioral models for PA output, (2.6), and dissipated power, (2.9), and the thermal impedance model introduced in Sec. 4.2. In this work, we assume there is a negligible reflection at the PA output. Therefore, single input models are sufficient for describing PA behaviors. However, the method can be extended for dual-input PA models without losing generality.

The algorithm starts with assigning initial temperature and input signal values. PA nonlinear behavioral models calculate the dissipated power and RF output signal at each time instant, t, given the input signal and temperature. The temperature for the next time instant is evaluated using the PA thermal impedance model and the dissipated power as the input. The new temperature value is utilized for evaluating the PA output at the next time instant, see Fig. 4.4. In this way, the algorithm calculates temperature-aware PA output for every time instant, following the modulation of the input signal excitation.

The dissipated power of a PA is mainly related to the output transistors. If we assume that dissipated power is equally distributed on output transistors, i.e.,

$n = 1, ..., N_{out}$, the effective PA temperature can be approximated as

$$P_{diss_i}(t) = \frac{P_{diss}(t)}{N_{out}} \qquad i = 1, ...N_{out}, \in \text{PA output transistors.} \tag{4.6}$$

where $P_{diss}(t)$ is the total dissipated power, and $P_{diss_i}(t)$ is the dissipated power in each output transistor. On the other hand, the output transistors' temperatures behave almost similar if they dissipate the same amount of power. Therefore, the PA temperature is approximated by

$$T(t) \approx \frac{\sum_{i=1}^{N_{out}} T_i(t)}{N_{out}} \approx T_i(t) \tag{4.7}$$

$$T_i(t) = \sum_{j=1}^{N_{out}} z_{imp,ij}(t) * P_{diss_j}(t) \tag{4.8}$$

where $z_{imp,ij}(t)$ are the elements of the thermal impulse response matrix, which can be obtained from (4.3) and $*$ is the convolution operator. Once the behavioral- and thermal impedance models are created, the proposed behavioral model-based electrothermal analysis can be implemented separately from the circuit simulator, in MATLAB or any computing tool. The proposed algorithm has, in this work, been used to evaluate the PA DUT performance under pulsed RF- and modulated signal excitations.

4.5 Electrothermal Characterization of a PA DUT

In this section, the proposed thermal modeling and electrothermal analysis approaches are applied to a PA DUT and validated through simulations by Keysight ADS Electro-Thermal solver and pulsed RF signal experiments, respectively. The ADS Electro-Thermal solver, which is called ADS-ETH for simplicity, is a fully coupled electrothermal tool that couples a 3-D FEM simulator, i.e., HeatWave, with its electrical solver [88] at each simulation point. The PA DUT is a two-stage class AB BiCMOS amplifier manufactured and provided by the NXP Semiconductors, see Fig. 4.5(a). The PA operates at 5-6 GHz and is equipped with sensing diodes for temperature monitoring.

4.5.1 PA DUT Thermal Impedance Model

The multi-port thermal impedance model and corresponding identification algorithms were introduced in Sec. 4.2. In this section, the thermal modeling results of the PA DUT are presented. In total, 123 individual areas were defined as heat sources, corresponding to active areas of the diodes and transistor fingers on the PA DUT

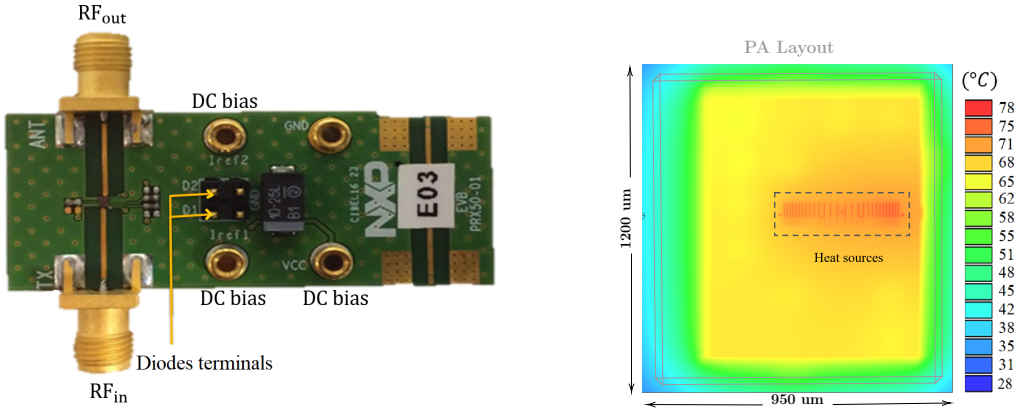

Figure 4.5: Thermal impedance identification of the PA DUT. a) Photo of the PA DUT evaluation board including temperature sensing diodes. b) Location and steady state temperature of heat sources on die obtained from ADS HeatWave 3D thermal simulator.

Table 4.1: Identified thermal time constants (in seconds) for the power amplifier device under test.

τ_1	τ_2	τ_3	τ_4	τ_5	τ_6	τ_7
1.70×10^{-8}	3.50×10^{-6}	1.60×10^{-7}	9.10×10^{-7}	9.00×10^{-6}	7.10×10^{-5}	2.30×10^{-4}
τ_8	τ_9	τ_{10}	τ_{11}	τ_{12}	τ_{13}	τ_{14}
6.10×10^{-4}	2.40×10^{-5}	1.73×10^{-2}	2.00×10^{-2}	1.60×10^{-3}	1.40×10^{-1}	$1.00 \times 10^{+1}$

layout. These areas correspond to the most power-consuming elements in the PA with the highest temperatures and are essential from the electrical viewpoint. The ADS Heatwave thermal simulator was used to extract the matrix of the PA thermal step response, see Algorithm 4.1. Fig. 4.5 (b) shows the steady-state temperature on the PA layout applying nominal DC dissipated power. The matrix of the thermal step response is obtained by exciting each heat source with a 20 mW step input power and collecting temperature rise on all heat source areas. The HeatWave simulation time was about 2 hours to extract 123×123 temperature step responses with a logarithmic time step setting.

Algorithm. 4.1 has converged to a 123×123 thermal impedance model of the PA DUT after 25 iterations which took 20 minutes to run on a regular PC. The algorithm converged to a thermal impedance model with 14 time constants common for all elements of the matrix. Fig. 4.6(a) presents the thermal simulation results compared with modeled results for $z_{th,ij}$ with $(i, j) = (11, 12), (1, 1), (1, 50)$ and $(1, 29)$. Fig. 4.6(b) shows the root mean square (RMS) error of the model identification, which is below 3 %. Table 4.1 shows the obtained values for time constants. The thermal problem is modeled to a 123×123 thermal impedance matrix.

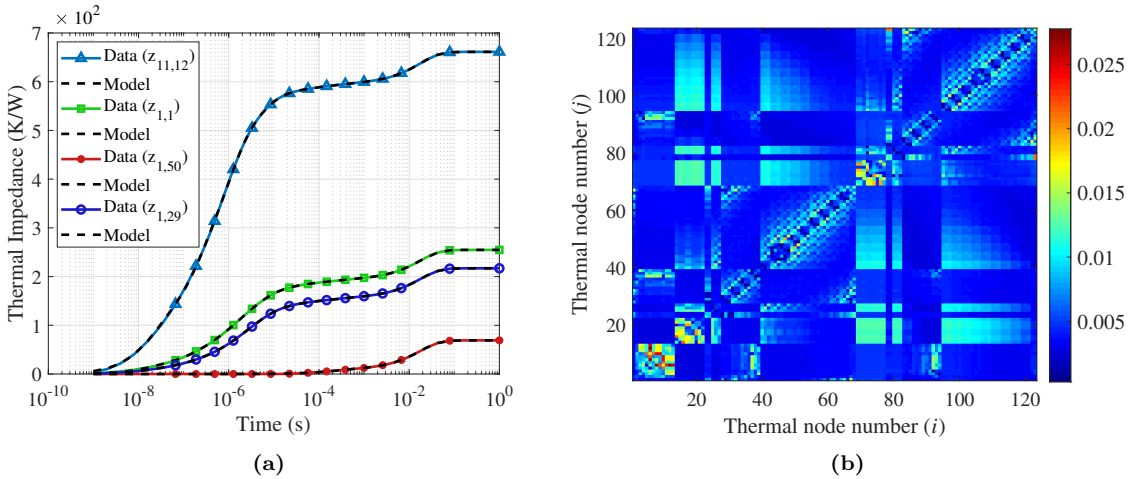

Figure 4.6: Thermal impedance identification of the PA DUT with each heat source excited with 20mW power step. a) Step responses for some of the elements. b) RMS error of the thermal model for all the elements of 123×123 thermal impedance matrix.

In Paper [C], the developed thermal impedance model is applied for electrothermal simulation of the PA DUT. The mathematical formulation of the thermal impedance matrix is directly used in the behavioral model-based electrothermal analysis approach. The PA DUT performance under pulsed RF signal excitations is evaluated using a behavioral model-based electrothermal analysis approach. The circuit-based electrothermal analysis approach, on the other hand, uses an equivalent thermal network extracted from the thermal model. The topology of the equivalent circuit is introduced in Sec. 4.3.

4.5.2 Electrothermal Circuit Simulation Results

In this section, transient and envelope circuit simulation results are presented to demonstrate the functionality of the proposed circuit-based electrothermal analysis method. The simulation results were verified by ADS-ETH simulations.

The PA DUT gain variation due to temperature rise was investigated using envelope simulations. Fig. 4.7 shows the dynamic gain of the PA DUT when the DC biases and RF input were switched on at $t = 2$ µs with 2 µs rise-time. From Fig. 4.7(a), it can be seen that, after 10 ms, the gain reduces about 0.4 dB due to the temperature rise.

Table. 4.2 compares the simulation time of the proposed method with ADS-ETH. Clearly, electrothermal circuit simulation using an equivalent thermal network is more efficient and faster but at the cost of an additional step for the thermal model identification. However, it is important to note that the thermal equivalent network, once extracted, can be reused for any simulation as long as the circuit layout is not changed. Furthermore, the thermal network extraction step can be added to circuit simulators such as ADS and Spice in an automated manner.

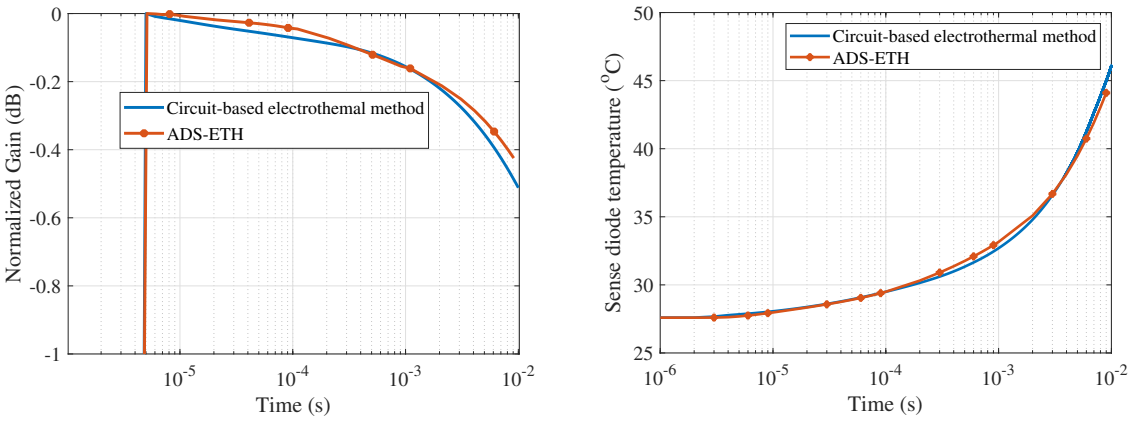

Figure 4.7: Results of envelop simulation obtained from the proposed circuit-based electrothermal method and ADS-ETH. The PA DUT is excited with an RF step power source with -20 dBm average power and 2 µs rise time and 2 µs delay. DC biases are also pulsed DC current and voltage sources with 2 µs delay and 2 µs rise time: a) Gain degradation, and b) temperature of the sensing diode versus time.

Table 4.2: Evaluation time per simulation point (seconds)

ADS solver	ADS-ETH	Circuit-based electrothermal
Transient simulation	122	0.001
Envelope simulation	107	0.200

4.5.3 Experimental Verification

The dynamic performance of the PA DUT has been evaluated by performing pulsed RF signal measurements and through behavioral model-based electrothermal analysis. The effect of temperature variations on the PA performance was observed as the PA kept heating and cooling synchronized with the input pulse.

Fig. 4.8 shows the block diagram of the experimental setup used for the pulsed characterization. The RF input signals were generated and captured at the PA output using a vector signal generator and a vector signal analyzer, respectively. The diode voltage, which is related to the PA temperature, was captured by an oscilloscope.

Static characterization

Fig. 4.9 compares the measured static AM/AM and PA drain efficiency with the behavioral model- and circuit-based simulation results. The circuit-based electrothermal results were obtained from ADS harmonic balance simulations, including

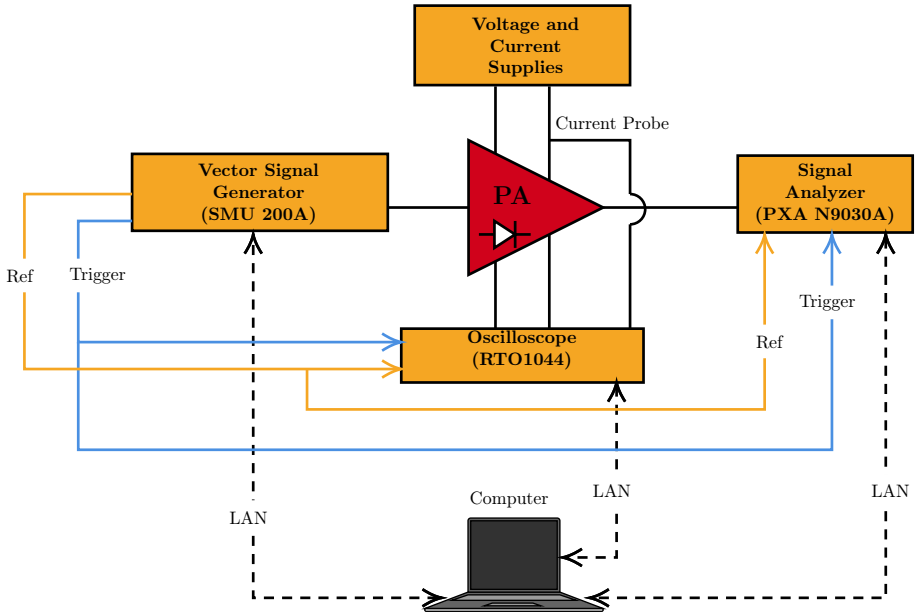

Figure 4.8: Block diagram of the pulsed measurement setup for evaluation of the proposed electrothermal methods. The PA is equipped with sensing diodes. The reference and trigger signals are required for correct pulse to pulse synchronization.

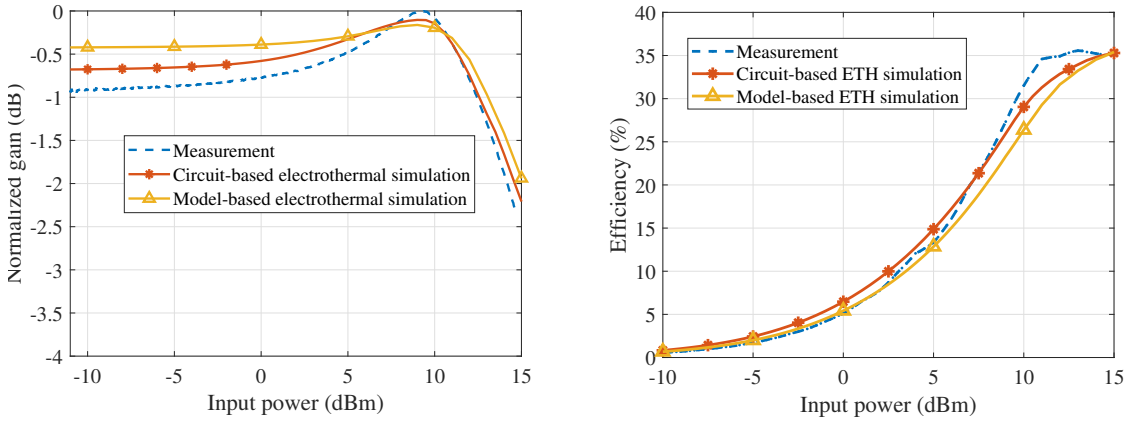

Figure 4.9: The PA measured a) AM/AM, b) drain efficiency, compared with the two proposed electrothermal analysis methods. The data is normalized to the maximum value of measured gain.

the thermal equivalent network. The behavioral model-based electrothermal simulation was performed following the proposed algorithm in Sec. 4.4.2 and by using the temperature-dependent nonlinear models of the PA DUT presented in Sec. 2.2.3. The static operating condition is emulated by running the behavioral model-based simulation for one second with $a = 0$ to reach the steady-state operating temperature in every modeled-based electrothermal analysis. Fig. 4.9 illustrates the excellent

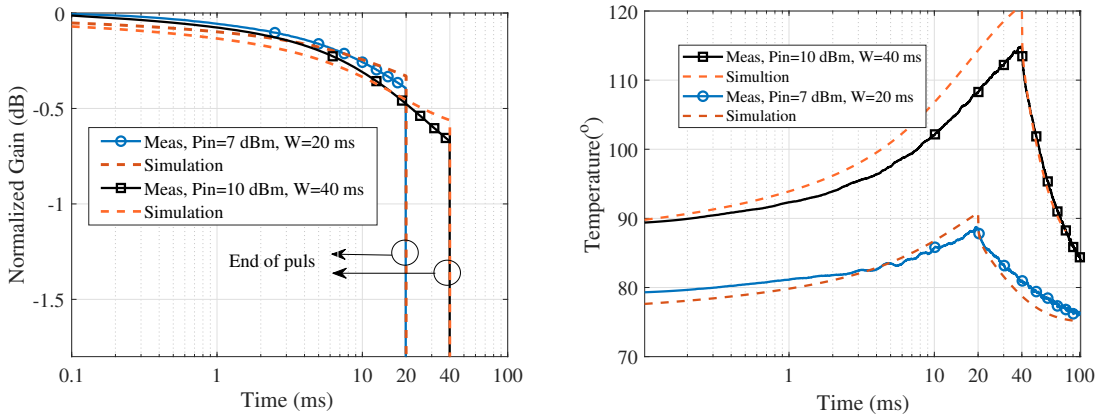

(a) **(b)**

Figure 4.10: Measured and simulated (Modeled-based) PA gain as well as temperature variation due to electrothermal effects. CW RF pulses with 20% duty cycle are applied to the PA DUT. a) PA normalized gain, b) temperature variation.

agreement between experimental and electrothermal simulation results of both static AM/AM and PA drain efficiency.

Pulsed RF characterization

The linearity of wireless systems with burst-type communication patterns must be very high and stable versus time. Furthermore, thermal issues adversely affect the PA static and dynamic gain characteristics. In particular, the dynamic variation of linearity is challenging to compensate using DPD techniques. Therefore, it is crucial to accurately characterize the PA dynamic linearity and gain under realistic pulsed RF excitation. In this section, the experimental and modeling results related to the pulsed RF signal measurements are presented. The measurement results, verified by modeled-based electrothermal analysis, evaluate the degradation of the PA dynamic performance due to thermal issues.

Fig. 4.10(a) presents the gain variations of the PA DUT under 20% duty-cycle input pulsed RF excitation. The results are related to two input pulses with on-state power of 7 dBm and 10 dBm and pulse widths of 20 and 40 ms, respectively. Fig. 4.10(b) shows the corresponding PA DUT temperature, measured using the embedded temperature sensing diode. It can be seen that the temperature of the PA DUT increases and decreases rapidly when the pulse is switched on and off, respectively. The temperature rises more if input pulse have higher input power. Moreover, the gain degradation at 40 ms is higher than 20 ms pulse because of the higher input power and more extended pulse width. The measured results adequately verified the behavioral model-based electrothermal analysis. It should be noted that simulations of long signal duration (such as burst communication signals) using the behavioral modeled-based method are much more efficient than applying envelope

simulation in the circuit-based electrothermal methods. In our case, the circuit-based electrothermal analysis even faced convergence issue and failed to simulate long signal sequences.

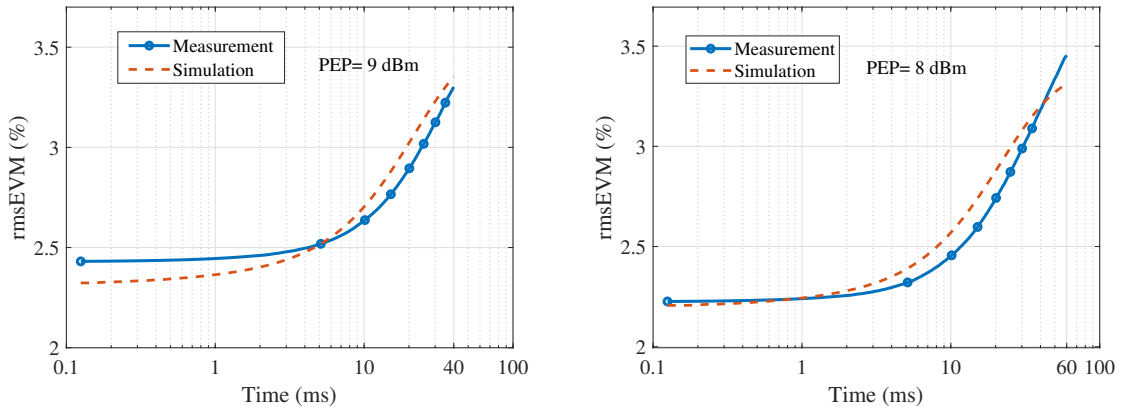

Figure 4.11: Simulated (Modeled-based) and measured PA EVM (RMS value%)versus time. Modulated signal pulses with a) 40 ms pulse-widths and Peak Envelope Power (PEP) of 9 dBm and, b) 60 ms pulse-widths 8 dBm PEP were injected to the PA input.

In another experiment, the PA DUT was excited with modulated pulses having 20 % duty-cycles 40 and 60 ms pulse-widths, respectively. The signal had a 64 QAM modulation scheme and 6 MHz bandwidth. Fig. 4.11 presents the RMS value of the measured Error Vector Magnitude (EVM) versus time, as calculated in 0.1 ms time frames. It can be seen that the EVM RMS value increased versus time due to temperature rise. Fig. 4.11 shows there is a good agreement between measured and simulated dynamic linearity.

4.6 Summary

Among other building blocks of active antenna transmitters, PAs have a temperature-dependent performance and dominate heat dissipation. Therefore, it is crucial to investigate their electrothermal behavior accurately. This chapter has dealt with efficient electrothermal modeling of the PA static and dynamic performance.

First, the thermal impedance matrix and joint linear and nonlinear fitting algorithms for model extraction have been introduced and explained. Two efficient methodologies for electrothermal characterization of PA ICs were proposed. The circuit-based electrothermal analysis method uses the equivalent thermal network incorporated with electrical circuit netlist for temperature-aware simulation of PAs. The behavioral model-based method combines the thermal impedance matrix of PAs and temperature-dependent behavioral models to predict PA performance, such as

dynamic linearity and gain. Overall, the simulation speed using thermal models was much faster than using coupled CAD solvers.

Experimental scenarios and results for validating the proposed thermal modeling method and electrothermal analysis approaches have been presented. The experimental results have validated the proposed methods and shown the effect of thermal issues on PA dynamic performance, such as gain variation and EVM.

Chapter 5

Conclusions

This thesis has addressed challenges related to the multidisciplinary analysis of active antenna transmitters for MIMO communication systems. At wireless communication systems, MIMO systems promise higher efficiency, higher capacity, and increased flexibility. MIMO systems utilize active antenna arrays at the transmitter side to increase the capacity and coverage of communication links. The performance analysis of any transmitter is crucial before implementing it. Analyzing active antenna transmitters requires the simulation of several subsystems, such as antenna arrays and power amplifiers, described by different physical models.

Because of the large number of antennas and PAs involved, analyzing an active antenna transmitter in MIMO systems is more challenging than traditional ones. In addition, the interaction between the antenna array and PAs is critical for mmWave transmitter modeling due to the high level of integration. This thesis combines the nonlinear load-pull-based PA model with antenna array characteristics in an iterative algorithm to model the active antenna transmitter performance. The transmitter model considers PA and antenna array interactions which are significant in mmWave active antenna transmitters. The accuracy of the proposed modeling approach has been validated using OTA measurements of a mmWave hybrid beamforming transmitter subarray module for different beam steering scenarios. The load-pull-based PA model is used to investigate the effect of coupling in a mmWave power combining module designed to provide higher power per antenna element in active antenna transmitters.

Thermal issues impact the transmitter performance dramatically. PAs are the primary source of power consumption, nonlinear distortion, and heat dissipation in transmitters. Therefore, an accurate prediction of transmitter behavior requires electrothermal analysis of PAs. This thesis has proposed efficient methodologies for thermal modeling and electrothermal analysis of PAs. The proposed methods combine an efficient thermal equivalent network, representing PA thermal behavior, with behavioral models of PA electrical performance. The proposed methods show considerably faster simulation speed than commercial electrothermal CAD tools, making it possible to analyze the PA and transmitter under realistic operating

conditions with dynamic modulated signal excitations. The proposed methods are validated using pulsed RF measurement. The static and dynamic experimental results reveal the importance of electrothermal analysis for the correct prediction of PA.

The proposed modeling approaches create possibilities for analyzing complex problems such as predicting active antenna transmitter performance and electrothermal simulation of PAs. This thesis shows that applying modeling techniques at the transmitter level is the key solution for predicting large-scale active antenna transmitters. Moreover, using the compact thermal model in combination with nonlinear behavioral models is efficient for electrothermal analysis of PAs. Therefore, this thesis shows the importance of modeling for the efficient analysis of transmitters and PAs. Extensive measurements scenarios and results adequately confirm the validity and functionality of proposed modeling approaches.

The proposed methodologies can be used to co-design, evaluate, and optimize active antenna transmitters with low computational effort. Also, they can provide design-guide for developing and optimizing antenna array and PAs to obtain higher efficiency and capacity in MIMO systems. Electrothermal modeling of PAs provides an essential tool for thermal management in PA and transmitters to reduce heat dissipation and increase efficiency. The proposed modeling approaches can be applied to understand better how individual building blocks must be co-designed for optimum performance of transmitters.

5.1 Future Work

The topic of modeling approaches for transmitter analysis still presents several possible directions for future work. A variety of investigations about how PA- and antenna array characteristics influence transmitter performance can be performed. These characteristics can include antenna array configuration, mismatch, and mutual coupling level, as well as PA nonlinearity and load-dependency. For instance, the effect of irregular and regular antenna arrays can be studied on the transmitter linearity. Such investigation can help in finding a suitable antenna array configuration for improving transmitter linearity performance. In general, such investigations can also provide design guides and criteria for developing antenna arrays and PAs for use in emerging active antenna array systems.

The proposed electrothermal analysis can be used to develop solutions to compensate for dynamic linearity and gain variations. The thermal model is developed assuming a linear thermal problem. However, for higher temperature variations, the thermal nonlinearity of materials appears. Thus the linear model becomes inaccurate. Developing a nonlinear thermal model, including power-dependent terms, is an exciting approach for the future extension of this work.

Finally, a model-based multiphysics analysis approach can be developed using the electrothermal model of a PA incorporated in the active antenna transmitter analysis

framework to investigate thermal effects in active antenna systems. Again, an efficient multiphysics analysis framework can perform various investigations related to PA and antenna array characteristics.

References

[1] P. Jonsson, "Ericsson mobility report," *Nov*, 2019.

[2] W. Roh *et al.*, "Millimeter-wave beamforming as an enabling technology for 5G cellular communications: Theoretical feasibility and prototype results," *IEEE Commun. Mag.*, vol. 52, no. 2, pp. 106–113, 2014.

[3] T. S. Rappaport *et al.*, "Millimeter wave mobile communications for 5G cellular: It will work!" *IEEE Access, 1*, pp. 335–349, 2013.

[4] Z. Pi and F. Khan, "An introduction to millimeter-wave mobile broadband systems," *IEEE Commun. Mag.*, vol. 49, no. 6, 2011.

[5] A. Ghosh, T. A. Thomas, M. C. Cudak, R. Ratasuk, P. Moorut, F. W. Vook, T. S. Rappaport, G. R. MacCartney, S. Sun, and S. Nie, "Millimeter-wave enhanced local area systems: A high-data-rate approach for future wireless networks," *IEEE J. Select. Areas Commun.*, vol. 32, no. 6, pp. 1152–1163, 2014.

[6] E. G. Larsson, O. Edfors, F. Tufvesson, and T. L. Marzetta, "Massive MIMO for next generation wireless systems," *IEEE Commun. Mag.*, vol. 52, no. 2, pp. 186–195, 2014.

[7] E. Bjornson, L. Van der Perre, S. Buzzi, and E. G. Larsson, "Massive MIMO in sub-6 GHz and mmwave: Physical, practical, and use-case differences," *IEEE Wireless Communications*, vol. 26, no. 2, pp. 100–108, 2019.

[8] M. E. Leinonen, N. Tervo, M. Jokinen, O. Kursu, and A. Pärssinen, "5G mmw link range uncertainties from RF system calculations and OTA measurements," *IEEE Access*, vol. 9, pp. 31 956–31 966, 2021.

[9] F. Sohrabi and W. Yu, "Hybrid analog and digital beamforming for mmWave OFDM large-scale antenna arrays," *IEEE J. Select. Areas Commun.*, vol. 35, no. 7, pp. 1432–1443, 2017.

[10] I. Ahmed, H. Khammari, A. Shahid, A. Musa, K. S. Kim, E. De Poorter, and I. Moerman, "A survey on hybrid beamforming techniques in 5G: Architecture

and system model perspectives," *IEEE Commun. Surv. & Tut.*, vol. 20, no. 4, pp. 3060–3097, 2018.

[11] A. Alkhateeb, O. El Ayach, G. Leus, and R. W. Heath, "Hybrid precoding for millimeter wave cellular systems with partial channel knowledge," in *Proc. Inf. Theo. Appl. Workshop (ITA)*, 2013, pp. 1–5.

[12] C. Fager, T. Eriksson, F. Barradas, K. Hausmair, T. Cunha, and J. C. Pedro, "Linearity and efficiency in 5G transmitters: New techniques for analyzing efficiency, linearity, and linearization in a 5G active antenna transmitter context," *IEEE Microw. Mag.*, vol. 20, no. 5, pp. 35–49, 2019.

[13] F. M. Barradas, P. M. Tomé, J. M. Gomes, T. R. Cunha, P. M. Cabral, and J. C. Pedro, "Power, linearity, and efficiency prediction for MIMO arrays with antenna coupling," *IEEE Transactions on Microwave Theory and Techniques*, vol. 65, no. 12, pp. 5284–5297, 2017.

[14] K. Hausmair, P. N. Landin, U. Gustavsson, C. Fager, and T. Eriksson, "Digital predistortion for multi-antenna transmitters affected by antenna crosstalk," *IEEE Trans. Microw. Theory Techn.*, vol. 66, no. 3, pp. 1524–1535, 2018.

[15] N. Tervo, M. E. Leinonen, J. Aikio, T. Rahkonen, and A. Pärssinen, "Analyzing the effects of PA variations on the performance of phased array digital predistortion," in *2018 IEEE 29th Annual International Symposium on Personal, Indoor and Mobile Radio Communications (PIMRC)*, 2018, pp. 215–219.

[16] A. Zaidi, F. Athley, J. Medbo, U. Gustavsson, G. Durisi, and X. Chen, *5G Physical Layer: principles, models and technology components.* Academic Press, 2018.

[17] X. Gu, D. Liu, C. Baks, O. Tageman, B. Sadhu, J. Hallin, L. Rexberg, and A. Valdes-Garcia, "A multilayer organic package with 64 dual-polarized antennas for 28GHz 5G communication," in *2017 IEEE MTT-S International Microwave Symposium (IMS)*, 2017, pp. 1899–1901.

[18] H. Aliakbari, A. Abdipour, A. Costanzo, D. Masotti, R. Mirzavand, and P. Mousavi, "Far-field-based nonlinear optimization of millimeter-wave active antenna for 5G services," *IEEE Trans. Microw. Theory Techn.*, vol. 67, no. 7, pp. 2985–2997, 2019.

[19] F. Ferranti, A. Magnani, V. d'Alessandro, S. Russo, N. Rinaldi, T. Dhaene, and M. de Magistris, "Effective electrothermal analysis of electronic devices and systems with parameterized macromodeling," *IEEE Transactions on Components, Packaging and Manufacturing Technology*, vol. 5, no. 6, pp. 788–796, 2015.

[20] V. Alessandro, M. de Magistris, A. Magnani, N. Rinaldi, and S. Russo, "Electrothermal macromodeling: an application to signal integrity analysis in highly integrated electronic systems," *IEEE Transactions on Components, Packaging and Manufacturing Technology*, vol. 3, no. 7, pp. 1237–1243, 2013.

[21] L. Codecasa, V. d'Alessandro, A. Magnani, N. Rinaldi, and P. J. Zampardi, "Fast novel thermal analysis simulation tool for integrated circuits (FANTASTIC)," in *20th International Workshop on Thermal Investigations of ICs and Systems*, 2014, pp. 1–6.

[22] C. Fager, X. Bland, K. Hausmair, J. Chani Cahuana, and T. Eriksson, "Prediction of smart antenna transmitter characteristics using a new behavioral modeling approach," in *2014 IEEE MTT-S International Microwave Symposium (IMS2014)*, 2014, pp. 1–4.

[23] S. K. Dhar, A. Abdelhafiz, M. Aziz, M. Helaoui, and F. M. Ghannouchi, "A reflection-aware unified modeling and linearization approach for power amplifier under mismatch and mutual coupling," *IEEE Trans. Microw. Theory Techn.*, no. 99, pp. 1–11, 2018.

[24] D. Lie, J. C. Mayeda, and J. Lopez, "Highly efficient 5G linear power amplifiers (pa) design challenges," in *2017 International Symposium on VLSI Design, Automation and Test (VLSI-DAT)*, 2017, pp. 1–3.

[25] P. M. Asbeck, N. Rostomyan, M. Özen, B. Rabet, and J. A. Jayamon, "Power amplifiers for mm-wave 5G applications: Technology comparisons and CMOS-SOI demonstration circuits," *IEEE Transactions on Microwave Theory and Techniques*, vol. 67, no. 7, pp. 3099–3109, 2019.

[26] C. Fager, K. Hausmair, T. Eriksson, and K. Buisman, "Analysis of thermal effects in active antenna array transmitters using a combined EM/circuit/thermal simulation technique," in *2015 Integrated Nonlinear Microwave and Millimetre-wave Circuits Workshop (INMMiC)*, 2015, pp. 1–3.

[27] E. Baptista, K. Buisman, J. C. Vaz, and C. Fager, "Analysis of thermal coupling effects in integrated MIMO transmitters," in *2017 IEEE MTT-S International Microwave Symposium (IMS)*, 2017, pp. 75–78.

[28] F. H. Raab, P. Asbeck, S. Cripps, P. B. Kenington, Z. B. Popovic, N. Pothecary, J. F. Sevic, and N. O. Sokal, "Power amplifiers and transmitters for RF and microwave," *IEEE Transactions on Microwave Theory and Techniques*, vol. 50, no. 3, pp. 814–826, 2002.

[29] F. M. Ghannouchi, O. Hammi, and M. Helaoui, *Behavioral modeling and predistortion of wideband wireless transmitters*. John Wiley & Sons, 2015.

[30] O. Hammi, S. Boumaiza, and F. M. Ghannouchi, "On the robustness of digital predistortion function synthesis and average power tracking for highly nonlinear power amplifiers," *IEEE Transactions on Microwave Theory and Techniques*, vol. 55, no. 6, pp. 1382–1389, 2007.

[31] N. Le Gallou, J. M. Nebus, E. Ngoya, and H. Buret, "Analysis of low frequency memory and influence on solid state HPA intermodulation characteristics," in *2001 IEEE MTT-S International Microwave Sympsoium Digest (Cat. No.01CH37157)*, vol. 2, 2001, pp. 979–982 vol.2.

[32] M. Isaksson, D. Wisell, and D. Ronnow, "A comparative analysis of behavioral models for RF power amplifiers," *IEEE Transactions on Microwave Theory and Techniques*, vol. 54, no. 1, pp. 348–359, 2006.

[33] J. C. Pedro and S. A. Maas, "A comparative overview of microwave and wireless power-amplifier behavioral modeling approaches," *IEEE Transactions on Microwave Theory and Techniques*, vol. 53, no. 4, pp. 1150–1163, 2005.

[34] D. M. Pozar, *Microwave engineering*. John wiley & sons, 2011.

[35] J. Wood, *Behavioral modeling and linearization of RF power amplifiers*. Artech House, 2014.

[36] A. Zhu and T. J. Brazil, "An overview of volterra series based behavioral modeling of RF/microwave power amplifiers," in *2006 IEEE Annual Wireless and Microwave Technology Conference*, 2006, pp. 1–5.

[37] J. Kim and K. Konstantinou, "Digital predistortion of wideband signals based on power amplifier model with memory," *Electronics Letters*, vol. 37, no. 23, pp. 1417–1418, 2001.

[38] D. R. Morgan, Z. Ma, J. Kim, M. G. Zierdt, and J. Pastalan, "A generalized memory polynomial model for digital predistortion of RF power amplifiers," *IEEE Transactions on Signal Processing*, vol. 54, no. 10, pp. 3852–3860, 2006.

[39] Lei Ding and G. T. Zhou, "Effects of even-order nonlinear terms on predistortion linearization," in *Proceedings of 2002 IEEE 10th Digital Signal Processing Workshop, 2002 and the 2nd Signal Processing Education Workshop.*, 2002, pp. 1–6.

[40] A. Abdelhafiz, L. Behjat, F. M. Ghannouchi, M. Helaoui, and O. Hammi, "A high-performance complexity reduced behavioral model and digital predistorter for MIMO systems with crosstalk," *IEEE Transactions on Communications*, vol. 64, no. 5, pp. 1996–2004, 2016.

[41] D. Saffar, N. Boulejfen, F. M. Ghannouchi, A. Gharsallah, and M. Helaoui, "Behavioral modeling of MIMO nonlinear systems with multivariable polynomials," *IEEE Transactions on Microwave Theory and Techniques*, vol. 59, no. 11, pp. 2994–3003, 2011.

[42] S. Amin, P. N. Landin, P. Händel, and D. Rönnow, "Behavioral modeling and linearization of crosstalk and memory effects in RF MIMO transmitters," *IEEE Trans. Microw. Theory Techn.*, vol. 62, no. 4, pp. 810–823, 2014.

[43] H. Zargar, A. Banai, and J. C. Pedro, "A new double input-double output complex envelope amplifier behavioral model taking into account source and load mismatch effects," *IEEE Transactions on Microwave Theory and Techniques*, vol. 63, no. 2, pp. 766–774, 2015.

[44] J. Cai, R. Gonçalves, and J. C. Pedro, "A new complex envelope behavioral model for load mismatched power amplifiers," *International Journal of RF and Microwave Computer-Aided Engineering*, vol. 27, no. 6, p. e21097, 2017.

[45] F. M. Barradas, T. R. Cunha, and J. C. Pedro, "Digital predistortion of RF PAs for MIMO transmitters based on the equivalent load," in *2017 Integrated Nonlinear Microwave and Millimetre-wave Circuits Workshop (INMMiC)*, 2017, pp. 1–4.

[46] H. Zargar, A. Banai, and J. C. Pedro, "DIDO behavioral model extraction setup using uncorrelated envelope signals," in *2015 European Microwave Conference (EuMC)*, 2015, pp. 646–649.

[47] C. Fager, K. Hausmair, K. Buisman, K. Andersson, E. Sienkiewicz, and D. Gustafsson, "Analysis of nonlinear distortion in phased array transmitters," in *Proc. Workshop Integ. Nonlinear Microw. Millim. Wave Circuits (INMMiC)*, Apr. 2017, pp. 1–4.

[48] D. Root *et al.*, "Polyharmonic distortion modeling," *IEEE Microw. Mag.*, vol. 7, no. 3, pp. 44–57, 2006.

[49] G. Z. El Nashef, F. Torres, S. Mons, T. Reveyrand, T. Monédière, E. Ngoya, and R. Quéré, "EM/circuit mixed simulation technique for an active antenna," *IEEE Antennas Wireless Propag. Lett.*, vol. 10, pp. 354–357, 2011.

[50] F. M. Ghannouchi and O. Hammi, "Behavioral modeling and predistortion," *IEEE Microwave Magazine*, vol. 10, no. 7, pp. 52–64, 2009.

[51] O. Hammi, F. M. Ghannouchi, S. Boumaiza, and B. Vassilakis, "A data-based nested LUT model for RF power amplifiers exhibiting memory effects," *IEEE Microwave and Wireless Components Letters*, vol. 17, no. 10, pp. 712–714, 2007.

[52] K. Rasilainen, K. Buisman, K. Andersson, and C. Fager, "Multi-physical simulations and modelling of an integrated GaN-on-Si module concept for millimetre-wave communications," in *2020 IEEE 70th Electronic Components and Technology Conference (ECTC)*, 2020, pp. 1369–1375.

[53] Y. Takayama, "A new load-pull characterization method for microwave power transistors," in *1976 IEEE-MTT-S International Microwave Symposium*, 1976, pp. 218–220.

[54] S. Gustafsson, M. Thorsell, and C. Fager, "A novel active load-pull system with multi-band capabilities," in *81st ARFTG Microwave Measurement Conference*, 2013, pp. 1–4.

[55] S. M. Kay, *Fundamentals of statistical signal processing*. Prentice Hall PTR, 1993.

[56] P. Kildal, *Foundations of Antennas: A Unified Approach*, 2015. [Online]. Available: http://www.kildal.se/

[57] C. A. Balanis, *Antenna Theory: Analysis and Design*. Wiley-Interscience, 2005.

[58] R. J. Mailloux, *Phased array antenna handbook*. Artech House antennas and propagation library, 2005.

[59] D. M. Pozar, "The active element pattern," *IEEE Trans. Antennas Propag.*, vol. 42, no. 8, pp. 1176–1178, 1994.

[60] D. Nopchinda and K. Buisman, "Measurement technique to emulate signal coupling between power amplifiers," *IEEE Transactions on Microwave Theory and Techniques*, vol. 66, no. 4, pp. 2034–2046, 2018.

[61] V. Rizzoli, A. Costanzo, D. Masotti, M. Aldrigo, F. Donzelli, and V. Degli Esposti, "Integration of non-linear, radiation, and propagation CAD techniques for MIMO link design," *J. Int. Microw. Wireless Tech.*, vol. 4, no. 2, pp. 223–232, 2012.

[62] V. Rizzoli, A. Costanzo, P. Spadoni, F. Donzelli, D. Masotti, and E. M. Vitucci, "A CAD procedure for MIMO link estimation by the combination of nonlinear, electromagnetic and propagation analysis techniques," in *Proc. IEEE MTT-S Int. Microw. Symp. Dig.*, 2008, pp. 927–930.

[63] M. Romier, A. Barka, H. Aubert, J.-P. Martinaud, and M. Soiron, "Load-pull effect on radiation characteristics of active antennas," *IEEE Antennas Wireless Propag. Lett.*, vol. 7, pp. 550–552, 2008.

[64] M. Joham, W. Utschick, and J. A. Nossek, "Linear transmit processing in MIMO communications systems," *IEEE Transactions on Signal Processing*, vol. 53, no. 8, pp. 2700–2712, 2005.

[65] H. Q. Ngo, *Massive MIMO: Fundamentals and system designs*. Linköping University Electronic Press, 2015, vol. 1642.

[66] K. Hausmair, S. Gustafsson, C. Sánchez-Pérez, P. N. Landin, U. Gustavsson, T. Eriksson, and C. Fager, "Prediction of nonlinear distortion in wideband active antenna arrays," *IEEE Transactions on Microwave Theory and Techniques*, vol. 65, no. 11, pp. 4550–4563, 2017.

[67] N. Tervo, B. Khan, O. Kursu, J. P. Aikio, M. Jokinen, M. E. Leinonen, M. Juntti, T. Rahkonen, and A. Pärssinen, "Digital predistortion of phased-array transmitter with shared feedback and far-field calibration," *IEEE Transactions on Microwave Theory and Techniques*, vol. 69, no. 1, pp. 1000–1015, 2021.

[68] ——, "Digital predistortion of millimeter-wave phased array transmitter with over-the-air calibrated simplified conductive feedback architecture," in *2020 IEEE/MTT-S International Microwave Symposium (IMS)*, 2020, pp. 543–546.

[69] E. Ng, Y. Beltagy, G. Scarlato, A. B. Ayed, P. Mitran, and S. Boumaiza, "Digital predistortion of millimeter-wave RF beamforming arrays using low number of steering angle-dependent coefficient sets," *IEEE Trans. Microw. Theory Techn.*, vol. 67, no. 11, pp. 4479–4492, 2019.

[70] L. Liu, W. Chen, L. Ma, and H. Sun, "Single-PA-feedback digital predistortion for beamforming MIMO transmitter," in *Proc. IEEE Int. Conf. Microw. Millim. Wave Tech. (ICMMT)*, vol. 2, 2016, pp. 573–575.

[71] C. Yu *et al.*, "Full-angle digital predistortion of 5G millimeter-wave massive MIMO transmitters," *IEEE Trans. Microw. Theory Techn.*, vol. 67, no. 7, pp. 2847–2860, 2019.

[72] X. Liu, *et al.*, "Beam-oriented digital predistortion for 5G massive MIMO hybrid beamforming transmitters," *IEEE Trans. Microw. Theory Techn.*, vol. 66, no. 7, pp. 3419–3432, 2018.

[73] S. Lee *et al.*, "Digital predistortion for power amplifiers in hybrid MIMO systems with antenna subarrays," in *Proc. IEEE 81st Veh. Tech. Conf. (VTC)*, 2015, pp. 1–5.

[74] M. Abdelaziz, L. Anttila, A. Brihuega, F. Tufvesson, and M. Valkama, "Digital predistortion for hybrid MIMO transmitters," *IEEE J. Selec. Topic on Signal Process*, vol. 12, no. 3, pp. 445–454, 2018.

[75] E. Ng, A. B. Ayed, P. Mitran, and S. Boumaiza, "Single-input single-output digital predistortion of multi-user RF beamforming arrays," in *IEEE MTT-S Int. Microw. Symp. (IMS)*, June 2019, pp. 472–475.

[76] E. Bryerton, M. Weiss, and Z. Popovic, "Efficiency of chip-level versus external power combining [microwave power amplifiers]," *IEEE Transactions on Microwave Theory and Techniques*, vol. 47, no. 8, pp. 1482–1485, 1999.

[77] B. Welp, K. Noujeim, and N. Pohl, "A wideband 20 to 28 GHz signal generator mmic with 30.8 dBm output power based on a power amplifier cell with 31% pae in SiGe," *IEEE Journal of Solid-State Circuits*, vol. 51, no. 9, pp. 1975–1984, 2016.

[78] A. Chakrabarti and H. Krishnaswamy, "High-power high-efficiency class-E-like stacked mmwave PAs in SOI and bulk CMOS: Theory and implementation," *IEEE Transactions on Microwave Theory and Techniques*, vol. 62, no. 8, pp. 1686–1704, 2014.

[79] C. Zhang, Z. Li, G. Cheng, H. Wang, and Z. Li, "A 26.5-40 GHz stacked power amplifier in 130 nm SiGe BiCMOS technology," in *2018 IEEE International Conference on Integrated Circuits, Technologies and Applications (ICTA)*. IEEE, 2018, pp. 36–37.

[80] Y. Chang, B.-Z. Lu, Y. Wang, and H. Wang, "A Ka-band stacked power amplifier with 24.8-dBm output power and 24.3% pae in 65-nm CMOS technology," in *2019 IEEE MTT-S International Microwave Symposium (IMS)*. IEEE, 2019, pp. 316–319.

[81] A. Roev, R. Maaskant, A. Höök, and M. Ivashina, "Wideband mm-wave transition between a coupled microstrip line array and siw for high-power generation mmics," *IEEE Microwave and Wireless Components Letters*, vol. 28, no. 10, pp. 867–869, 2018.

[82] M. Pedram and S. Nazarian, "Thermal modeling, analysis, and management in VLSI circuits: Principles and methods," *Proceedings of the IEEE*, vol. 94, no. 8, pp. 1487–1501, 2006.

[83] M. T. Ozalas, "The impact of electro-thermal coupling on HBT power amplifiers," in *2014 IEEE Compound Semiconductor Integrated Circuit Symposium (CSICS)*, 2014, pp. 1–4.

[84] S. Wunsche, C. Clauss, P. Schwarz, and F. Winkler, "Electro-thermal circuit simulation using simulator coupling," *IEEE Transactions on Very Large Scale Integration (VLSI) Systems*, vol. 5, no. 3, pp. 277–282, 1997.

[85] W. van Petegem, B. Geeraerts, W. Sansen, and B. Graindourze, "Electrothermal simulation and design of integrated circuits," *IEEE Journal of Solid-State Circuits*, vol. 29, no. 2, pp. 143–146, 1994.

[86] A. Chvála, D. Donoval, A. Šatka, M. Molnár, J. Marek, and P. Príytný, "Advanced methodology for fast 3-D TCAD device/circuit electrothermal simulation and analysis of power HEMTs," *IEEE Transactions on Electron Devices*, vol. 62, no. 3, pp. 828–834, 2015.

[87] A. Chvála, D. Donoval, J. Marek, P. Príytný, M. Molnár, and M. Mikolášek, "Fast 3-D electrothermal device/circuit simulation of power superjunction MOSFET based on SDevice and HSPICE interaction," *IEEE Transactions on Electron Devices*, vol. 61, no. 4, pp. 1116–1122, 2014.

[88] "ADS electro-thermal simulator." [Online]. Available: https://www.keysight.com/se/en/product/W2349EP/pathwave-ads-electro-thermal-simulator-element.html

[89] V. Košel, S. de Filippis, L. Chen, S. Decker, and A. Irace, "FEM simulation approach to investigate electro-thermal behavior of power transistors in 3-D," *Microelectronics Reliability*, vol. 53, no. 3, pp. 356–362, 2013. [Online]. Available: https://www.sciencedirect.com/science/article/pii/S0026271412004167

[90] L. Codecasa, "Thermal networks from heat wave equation," *IEEE Transactions on components and packaging technologies*, vol. 28, no. 1, pp. 14–22, 2005.

[91] ——, "Compact models of dynamic thermal networks with many heat sources," *IEEE Transactions on Components and Packaging Technologies*, vol. 30, no. 4, pp. 653–659, 2007.

[92] J. T. Hsu and L. Vu-Quoc, "A rational formulation of thermal circuit models for electrothermal simulation. I. finite element method [power electronic systems]," *IEEE Transactions on Circuits and Systems I: Fundamental Theory and Applications*, vol. 43, no. 9, pp. 721–732, 1996.

[93] ——, "A rational formulation of thermal circuit models for electrothermal simulation. II. model reduction techniques [power electronic systems]," *IEEE Transactions on Circuits and Systems I: Fundamental Theory and Applications*, vol. 43, no. 9, pp. 733–744, 1996.

[94] R. Sommet, D. Lopez, and R. Quere, "From 3d thermal simulation of hbt devices to their thermal model integration into circuit simulators via ritz vectors reduction technique," in *ITherm 2002. Eighth Intersociety Conference on Thermal and Thermomechanical Phenomena in Electronic Systems (Cat. No.02CH37258)*, 2002, pp. 22–28.

[95] L. Codecasa, D. D'Amore, and P. Maffezzoni, "An Arnoldi based thermal network reduction method for electro-thermal analysis," *IEEE Transactions on Components and Packaging Technologies*, vol. 26, no. 1, pp. 186–192, 2003.

[96] L. Codecasa, D. D'Amore, P. Maffezzoni, and W. Batty, "Analytical multipoint moment matching reduction of distributed thermal networks," *IEEE Transactions on Components and Packaging Technologies*, vol. 27, no. 1, pp. 87–95, 2004.

[97] L. Codecasa, D. D'Amore, and P. Maffezzoni, "Multipoint moment matching reduction from port responses of dynamic thermal networks," *IEEE Transactions on Components and Packaging Technologies*, vol. 28, no. 4, pp. 605–614, 2005.

[98] P. Mathai and B. Shapiro, "Interconnection of subsystem reduced-order models in the electrothermal analysis of large systems," *IEEE Transactions on Components and Packaging Technologies*, vol. 30, no. 2, pp. 317–329, 2007.

[99] L. Codecasa, V. d'Alessandro, A. Magnani, and A. Irace, "Circuit-based electrothermal simulation of power devices by an ultrafast nonlinear MOR approach," *IEEE Transactions on Power Electronics*, vol. 31, no. 8, pp. 5906–5916, 2016.

[100] L. Codecasa, D. D'Amore, and P. Maffezzoni, "Compact modeling of electrical devices for electrothermal analysis," *IEEE Transactions on Circuits and Systems I: Fundamental Theory and Applications*, vol. 50, no. 4, pp. 465–476, 2003.

[101] ——, "Compact thermal networks for modeling packages," *IEEE Transactions on Components and Packaging Technologies*, vol. 27, no. 1, pp. 96–103, 2004.

[102] M. Rencz, V. Szekely, and A. Poppe, "A methodology for the co-simulation of dynamic compact models of packages with the detailed models of boards," *IEEE Transactions on Components and Packaging Technologies*, vol. 30, no. 3, pp. 367–374, 2007.

[103] C. Lasance, "Recent progress in compact thermal models," in *Ninteenth Annual IEEE Semiconductor Thermal Measurement and Management Symposium, 2003.*, 2003, pp. 290–299.

[104] L. Codecasa, "Canonical forms of one-port passive distributed thermal networks," *IEEE Transactions on Components and Packaging Technologies*, vol. 28, no. 1, pp. 5–13, 2005.

[105] *HSPICE®User Guide: Basic Simulation and Analysis, Version J-2014.09*, Synopsys, September 2014.